Pressure-anisotropy-induced nonlinearities in the kinetic magnetorotational instability

J. Squire[1,2,†], E. Quataert[3] and M. W. Kunz[4,5]

[1]TAPIR, Mailcode 350-17, California Institute of Technology, Pasadena, CA 91125, USA

[2]Walter Burke Institute for Theoretical Physics, Pasadena, CA 91125, USA

[3]Astronomy Department and Theoretical Astrophysics Center, University of California, Berkeley, CA 94720, USA

[4]Department of Astrophysical Sciences, Princeton University, Peyton Hall, Princeton, NJ 08544, USA

[5]Princeton Plasma Physics Laboratory, PO Box 451, Princeton, NJ 08543, USA

In collisionless and weakly collisional plasmas, such as hot accretion flows onto compact objects, the magnetorotational instability (MRI) can differ significantly from the standard (collisional) MRI. In particular, pressure anisotropy with respect to the local magnetic-field direction can both change the linear MRI dispersion relation and cause nonlinear modifications to the mode structure and growth rate, even when the field and flow perturbations are very small. This work studies these pressure-anisotropy-induced nonlinearities in the weakly nonlinear, high-ion-beta regime, before the MRI saturates into strong turbulence. Our goal is to better understand how the saturation of the MRI in a low-collisionality plasma might differ from that in the collisional regime. We focus on two key effects: (i) the direct impact of self-induced pressure-anisotropy nonlinearities on the evolution of an MRI mode, and (ii) the influence of pressure anisotropy on the 'parasitic instabilities' that are suspected to cause the mode to break up into turbulence. Our main conclusions are: (i) The mirror instability regulates the pressure anisotropy in such a way that the linear MRI in a collisionless plasma is an approximate nonlinear solution once the mode amplitude becomes larger than the background field (just as in magnetohyrodynamics). This implies that differences between the collisionless and collisional MRI become unimportant at large amplitudes. (ii) The break up of large-amplitude MRI modes into turbulence via parasitic instabilities is similar in collisionless and collisional plasmas. Together, these conclusions suggest that the route to magnetorotational turbulence in a collisionless plasma may well be similar to that in a collisional plasma, as suggested by recent kinetic simulations. As a supplement to these findings, we offer guidance for the design of future kinetic simulations of magnetorotational turbulence.

Key words: astrophysical plasmas, plasma instabilities, plasma nonlinear phenomena

---

† Email address for correspondence: jsquire@caltech.edu

1. Introduction

Across a wide variety of accreting astrophysical systems, the inflow of matter is thought to rely on turbulent angular-momentum transport driven by the magnetorotational instability (MRI; Balbus & Hawley 1991, 1998). The majority of works studying the MRI, in particular its saturation into turbulence (e.g. Hawley, Gammie & Balbus 1995; Hawley, Balbus & Stone 2001; Ryan *et al.* 2017), have been based on magnetohydrodynamics (MHD). They thus implicitly assume that the collisional mean free path of gas particles is small in comparison to the scales of all fluid motions. However, this assumption can be far from valid in many accreting systems. For instance, in radiatively inefficient accretion flows onto supermassive black holes (RIAFs; see Narayan, Mahadevan & Quataert 1998; Hawley & Balbus 2002; Quataert 2003; Yuan & Narayan 2014), a large portion of the gravitational potential energy of the infalling gas is converted directly into thermal energy, suggesting ion temperatures $T_i \sim 10^{12}$ K with corresponding ion collisional mean free paths that are orders of magnitude larger than the system size.

As shown by Quataert, Dorland & Hammett (2002) (hereafter Q02), Sharma, Hammett & Quataert (2003) and Balbus (2004), the linear magnetorotational instability still exists in collisionless and weakly collisional plasmas. This kinetic MRI (KMRI) has seen subsequent theoretical attention. As well as extensions to the original linear analyses using either fully kinetic treatments (Sharma *et al.* 2003; Heinemann & Quataert 2014; Quataert, Heinemann & Spitkovsky 2015) or fluid models (Ferraro 2007; Rosin & Mestel 2012), various works have explored turbulent transport in the fully nonlinear regime, generally finding behaviour that bears a strong similarity to that seen in standard resistive MHD. Sharma *et al.* (2006) (hereafter S06) was the first to study MRI turbulence in this regime using a kinetically motivated fluid closure, an approach that has been followed in a variety of works since (e.g. Sharma *et al.* 2007; Chandra *et al.* 2015; Foucart *et al.* 2015). Recently, it has become possible to study the MRI using truly kinetic particle-in-cell (PIC) methods, both in two dimensions (Riquelme *et al.* 2012; Hoshino 2013; Kunz, Stone & Bai 2014*b*) and three dimensions (Hoshino 2015; Kunz, Stone & Quataert 2016). Most notably, in Kunz *et al.* (2016), a fully collisionless plasma was seen to develop into MRI turbulence with strong similarities to that seen in comparable MHD calculations (or, even more so, similarities to the model of S06), providing a fascinating example of a fully collisionless plasma behaving as a collisional fluid.

In this paper, we explore the regime between fully nonlinear turbulence and the linear KMRI. Our purpose is to move towards understanding the nonlinear saturation of the KMRI, in particular the similarities with, and differences to, the standard MRI. Our philosophy is to examine the simplest (and, hopefully, the most significant) modifications to MHD. With this in mind, we consider both the kinetically motivated Landau-fluid (LF) model used by S06 and 'Braginskii' MHD (Braginskii 1965), which is valid in the weakly collisional regime. We study two interlinked effects, each of which could have a strong influence on how the KMRI saturates into turbulence. The first effect is the pressure anisotropy (Δp) driven by growing KMRI modes. This can nonlinearly affect the modes' evolution (even in one dimension) at amplitudes far smaller – by a factor $\sim \beta$, the ratio of thermal to magnetic pressure – than occurs in a standard compressible gas with isotropic pressure. It is important to understand the effect of this nonlinearity, because it is these anisotropy-modified KMRI modes that will be disrupted at large amplitudes and excite turbulence. The second effect that we study is the nonlinear disruption of KMRI modes by parasitic modes, which are thought to govern the transition into strong turbulence (Goodman & Xu 1994;

Latter, Lesaffre & Balbus 2009; Pessah & Goodman 2009; Latter, Fromang & Gressel 2010; Longaretti & Lesur 2010). MHD parasitic modes are Kelvin–Helmholtz and tearing modes that feed off strong gradients in the large-amplitude MRI 'channel' mode.[1] A significant difference in parasitic-mode growth rates in a collisionless plasma (compared to MHD) would suggest that the saturation of the KMRI into turbulence would also be significantly modified, perhaps with important implications for KMRI-driven turbulence.

Our main results are twofold. First, once the KMRI channel mode amplitude δB surpasses the strength of the background field B_0, its evolution always reverts to MHD-like behaviour. In particular, because of the pressure-anisotropy-limiting effects of kinetic microinstabilities (Schekochihin *et al.* 2008; Kunz *et al.* 2015) and the specific form of MRI modes, the pressure anisotropy has very little effect on mode evolution once $\delta B \gtrsim B_0$. The MRI modes are then approximate nonlinear solutions of the Landau-fluid or Braginskii models until they reach very large amplitudes. However, at moderate mode amplitudes $\delta B \lesssim B_0$, the effect of pressure anisotropy can be significant; for example, it causes strong modifications to the KMRI in the presence of a background azimuthal field[2] at amplitudes well below where it would saturate into turbulence. Our second result is that there is not a strong difference in parasitic-mode growth rates between the kinetic and MHD models, which indicates that modes can grow to similar amplitudes before being disrupted in collisionless and collisional systems. Together these conclusions suggest that the saturation of MRI modes into turbulence in high-β collisionless and weakly collisional regimes will be similar to what occurs in a collisional (MHD) plasma. This appears to be the case in the simulations that have been run up to now, including those that do not rely on fluid closure schemes (Riquelme *et al.* 2012; Hoshino 2013, 2015; Kunz *et al.* 2016).

In some ways, the results of this work will primarily be of interest for understanding and designing future three-dimensional (3-D) fully kinetic simulations of MRI turbulence. Such simulations are the only clear method available to explore the collisionless accretion flows without *ad hoc* assumptions, but are very demanding computationally. The primary difficulty arises from the enormous scale separation in RIAFs between the ion gyrofrequency Ω_i (which must be resolved in a kinetic code) and the disk rotation frequency Ω. Simulations are necessarily limited to modest values of Ω_i/Ω, and it is thus crucial to understand some of the basic differences between the MRI and KMRI in designing and analysing simulations, so as to ensure that observed effects are not an artefact of limited scale separation. To add to these difficulties, our understanding of the processes governing even the simplest MHD MRI turbulence remains somewhat limited (e.g. see Fromang *et al.* 2007; Lesur & Longaretti 2007; Fromang & Stone 2009; Blackman 2012; Simon, Beckwith & Armitage 2012; Meheut *et al.* 2015; Squire & Bhattacharjee 2016).

The remainder of the paper is organized as follows. In § 2 we introduce the models used throughout our work and the numerical methods used to solve them (§ 2.2). Because the effects that arise due to pressure anisotropy may be unfamiliar to many readers, we provide a brief account in § 2.3 of the primary differences between each model and MHD. One-dimensional nonlinearities arising due to self-generated pressure anisotropies are then treated in § 3, starting with an overview of the linear physics, and then treating the pure-vertical-field KMRI (§ 3.2) and azimuthal-field KMRI (§ 3.3) separately. An overview of these results is given in § 3.4. We then

---

[1]The azimuthally and radially constant MRI modes are often termed 'channel modes' because they are able to survive unmodified to very large amplitudes.

[2]This is sometimes termed the magnetoviscous instability (MVI), following Balbus (2004).

consider the evolution of parasitic modes in § 4, starting with linear calculations on sinusoidal background profiles (§ 4.1) and then showing fully nonlinear calculations using the ZEUS code used by S06 (§ 4.2). This section is deliberately kept brief, due to the null result that nonlinear saturation is not strongly affected by the pressure anisotropy. A discussion of kinetic effects neglected in our model is given in § 5. We then combine our results with those from previous kinetics simulations of mirror and magnetorotational instabilities to provide guidance for the design of future simulations of KMRI turbulence (§ 6). Finally, we conclude with a summary in § 7.

2. Governing equations: the effects of pressure anisotropy

Our philosophy throughout this work is to consider the simplest and most general modifications to MRI evolution on the largest (MHD) scales due to kinetic physics. We anticipate (but cannot prove) that these are the most important kinetic modifications to the MRI. We thus focus on the development of a gyrotropic pressure anisotropy – i.e. a pressure tensor that differs in the directions parallel ($p_\parallel$) and perpendicular ($p_\perp$) to the magnetic-field lines, but that is unchanged by rotations about the field line. This pressure anisotropy, $\Delta p \equiv p_\perp - p_\parallel$, causes an additional stress in the momentum equation, which can nonlinearly affect the MRI modes at much lower amplitudes than occurs in standard MHD. The gyrotropic approximation is generally valid when the magnetic field varies on spatial and temporal scales much larger than the ion gyroradius and inverse gyrofrequency.

2.1. *Basic equations and closure models*

Our equations are obtained as follows. A small patch of an accretion disc, co-orbiting with a fiducial point R_0 in the mid-plane of the unperturbed disc at an angular velocity $\boldsymbol{\Omega} = \Omega \hat{\boldsymbol{z}}$, is represented in Cartesian coordinates with the x and y directions corresponding to the radial and azimuthal directions, respectively. Differential rotation is accounted for by including the Coriolis force and by imposing a background linear shear flow, $\boldsymbol{U}_0 = -Sx\hat{\boldsymbol{y}}$, where $S \equiv -\mathrm{d}\Omega/\mathrm{d}\ln R_0 > 0$ is the shear frequency; Keplerian rotation yields $S = (3/2)\Omega$. The evolutionary equations for the first three moments of the plasma distribution function are then (Chew, Goldberger & Low 1956; Kulsrud 1983; Schekochihin *et al.* 2010),

$$\frac{\mathrm{d}\rho}{\mathrm{d}t} = -\rho \boldsymbol{\nabla} \cdot \boldsymbol{u}, \tag{2.1}$$

$$\rho \left(\frac{\mathrm{d}\boldsymbol{u}}{\mathrm{d}t} + 2\Omega\hat{\boldsymbol{z}} \times \boldsymbol{u} - 2S\Omega x\hat{\boldsymbol{x}} \right) = -\boldsymbol{\nabla} \left(p_\perp + \frac{B^2}{8\pi} \right) + \boldsymbol{\nabla} \cdot \left[\hat{\boldsymbol{b}}\hat{\boldsymbol{b}} \left(\frac{B^2}{4\pi} + \Delta p \right) \right], \tag{2.2}$$

$$\frac{\mathrm{d}\boldsymbol{B}}{\mathrm{d}t} = \boldsymbol{B} \cdot \boldsymbol{\nabla}\boldsymbol{u} - \boldsymbol{B}\boldsymbol{\nabla} \cdot \boldsymbol{u}, \tag{2.3}$$

$$\frac{\mathrm{d}p_\perp}{\mathrm{d}t} = -\boldsymbol{\nabla} \cdot (q_\perp \hat{\boldsymbol{b}}) - q_\perp \boldsymbol{\nabla} \cdot \hat{\boldsymbol{b}} + p_\perp \hat{\boldsymbol{b}}\hat{\boldsymbol{b}} : \boldsymbol{\nabla}\boldsymbol{u} - 2p_\perp \boldsymbol{\nabla} \cdot \boldsymbol{u} - \nu_c \Delta p, \tag{2.4}$$

$$\frac{\mathrm{d}p_\parallel}{\mathrm{d}t} = -\boldsymbol{\nabla} \cdot (q_\parallel \hat{\boldsymbol{b}}) + 2q_\perp \boldsymbol{\nabla} \cdot \hat{\boldsymbol{b}} - 2p_\parallel \hat{\boldsymbol{b}}\hat{\boldsymbol{b}} : \boldsymbol{\nabla}\boldsymbol{u} - p_\parallel \boldsymbol{\nabla} \cdot \boldsymbol{u} + 2\nu_c \Delta p, \tag{2.5}$$

where $\mathrm{d}/\mathrm{d}t \equiv \partial/\partial t + \boldsymbol{u} \cdot \boldsymbol{\nabla}$ is the convective derivative. The velocity $\boldsymbol{u}$ in (2.1)–(2.5) includes both the background shear flow $\boldsymbol{U}_0$ and perturbations on top of this $\delta\boldsymbol{u}$ (e.g. the MRI). The other symbols have their usual meanings: ρ is the mass density, $\boldsymbol{B}$ is the magnetic field, ν_c is the particle collision frequency, while $B \equiv |\boldsymbol{B}|$ and $\hat{\boldsymbol{b}} \equiv \boldsymbol{B}/B$

denote the magnetic-field strength and direction (note that $\nabla \cdot (\hat{\boldsymbol{b}}\hat{\boldsymbol{b}}B^2)$ is simply $\boldsymbol{B} \cdot \nabla \boldsymbol{B}$). The pressures perpendicular and parallel to $\hat{\boldsymbol{b}}$ are $p_\perp$ and $p_\parallel$ respectively, while $q_\perp$ and $q_\parallel$ denote the fluxes of perpendicular and parallel heat in the direction parallel to $\hat{\boldsymbol{b}}$. Note that $p_\perp$ and $p_\parallel$ in (2.2) should in principle be summed over both particle species (with separate pressures for each species), while ρ and $\boldsymbol{u}$ in (2.1)–(2.3) are the ion density and flow velocity. For simplicity, in this work we solve only the ion pressure equations (i.e. $p_\perp = p_{\perp,i}$, $p_\parallel = p_{\parallel,i}$), which is justified in the limit of cold electrons (as expected in RIAFs, e.g. Sharma *et al.* 2007). We have also neglected non-ideal corrections to the induction equation (2.3) (e.g. the Hall term), which is appropriate given our neglect of finite Larmor radius (FLR) effects in (2.2) (we will, however, include a hyper-resistivity term in equation (2.3) for numerical reasons; see § 2.2). For convenience, we define the dimensionless anisotropy $\Delta \equiv \Delta p/p_0$, where $p_0 = (p_\perp + 2p_\parallel)/3$ is the total thermal pressure, as well as the ratio of thermal to magnetic pressure $\beta \equiv 8\pi p_0/B^2$, the Alfvén speed $v_A = B/\sqrt{4\pi\rho}$ and its $\hat{z}$ component $v_{Az} = B_z/\sqrt{4\pi\rho}$, the sound speed $c_s = \sqrt{p_0/\rho}$ and the parallel sound speed $c_{s\parallel} = \sqrt{p_\parallel/\rho}$. The double-dot notation used in (2.4)–(2.5) and throughout this work is $\hat{\boldsymbol{b}}\hat{\boldsymbol{b}} : \nabla \boldsymbol{u} \equiv \sum_{i,j} b_i b_j \partial_i u_j$.

In their present form, equations (2.1)–(2.5) are not closed, due to the presence of the unspecified heat fluxes, $q_\perp$ and $q_\parallel$. These must be either specified using a closure scheme, neglected or solved for using the full kinetic equations. In this work we consider three closures for $q_\perp$ and $q_\parallel$ (or equivalently, three approximations to (2.4)–(2.5)). These will be seen to lead to quite different behaviour in solutions of (2.1)–(2.5). They are:

Collisionless Landau-fluid closure. Landau-fluid (LF) closures have been used extensively in the fusion community (Hammett & Perkins 1990; Hammett, Dorland & Perkins 1992; Snyder, Hammett & Dorland 1997) and, to a lesser degree, for astrophysical applications (S06; Sharma *et al.* 2007). They are particularly well suited for modelling collisionless ($\nu_c = 0$) plasmas. In the LF closure, the heat fluxes,

$$q_\perp = -\frac{2c_{s\parallel}^2}{\sqrt{2\pi}c_{s\parallel}|k_\parallel| + \nu_c} \left[\rho\nabla_\parallel \left(\frac{p_\perp}{\rho} \right) - p_\perp \left(1 - \frac{p_\perp}{p_\parallel} \right) \frac{\nabla_\parallel B}{B} \right], \qquad (2.6)$$

$$q_\parallel = -\frac{8c_{s\parallel}^2}{\sqrt{8\pi}c_{s\parallel}|k_\parallel| + (3\pi - 8)\nu_c} \rho\nabla_\parallel \left(\frac{p_\parallel}{\rho} \right), \qquad (2.7)$$

are constructed to replicate the effects of linear Landau damping. Here $\nabla_\parallel \equiv \hat{\boldsymbol{b}} \cdot \nabla$ denotes the gradient parallel to the field and $|k_\parallel|$ denotes the wavenumber parallel to the field, which must be considered as an operator because it appears in the denominator of (2.6)–(2.7). The forms of the heat fluxes in (2.6)–(2.7) accurately reproduce the true kinetic growth rates and frequencies for a variety of large-scale (MHD) modes, including the MRI (Q02; Sharma *et al.* 2003). We refer the reader to Snyder *et al.* (1997) and S06 for more information.

Weakly collisional 'Braginskii' closure. In the Braginskii regime, $|\nabla \boldsymbol{u}| \ll \nu_c$ (Braginskii 1965), the pressure anisotropy is strongly influenced by collisional relaxation. We thus neglect $d_t p_\perp$ and $d_t p_\parallel$ in (2.4)–(2.5) and balance the double-adiabatic production of pressure anisotropy (the $\hat{\boldsymbol{b}}\hat{\boldsymbol{b}} : \nabla \boldsymbol{u}$ and $\nabla \cdot \boldsymbol{u}$ terms) against its collisional relaxation (the $\nu_c \Delta p$ terms) to find

$$\Delta \approx \frac{1}{\nu_c} \left(\hat{\boldsymbol{b}}\hat{\boldsymbol{b}} : \nabla \boldsymbol{u} - \frac{1}{3}\nabla \cdot \boldsymbol{u} \right) = \frac{1}{\nu_c} \frac{d}{dt} \ln \frac{B}{\rho^{2/3}}, \qquad (2.8)$$

where we have also used the fact that $\nu_c/|\nabla \boldsymbol{u}| \gg 1$ implies $\Delta p \ll p_0$. (For $\beta \gg 1$, the $\nabla \cdot \boldsymbol{u}$ term can also be neglected.) When inserted into the momentum equation (2.2), equation (2.8) has the form of an anisotropic viscous stress, and is thus referred to as 'Braginskii viscosity' (or Braginskii MHD for the full set of equations). Note that we have neglected heat fluxes in arriving at (2.8), a simplification that is rigorously obtained if $\nu_c/|\nabla \boldsymbol{u}| \gg \beta^{1/2}$ (the 'high-collisionality' regime). On the other hand, if $\nu_c/|\nabla \boldsymbol{u}| \ll \beta^{1/2}$ (the 'moderate-collisionality' regime), the heat fluxes are strong over the time scales of the motion (Mikhailovskii & Tsypin 1971), and their contribution to the (ion) pressure anisotropy must be retained. (See § B.4 for further discussion.) In this case, there is no simple closure that can be devised (e.g. see appendix B of Squire, Schekochihin & Quataert 2017) and it is usually easier to consider the full LF system.

Double-adiabatic closure. The double-adiabatic, or Chew–Goldberger–Low (CGL), closure (Chew *et al.* 1956) simply involves setting $q_\perp = q_\parallel = 0$. This approximation is far from justified for subsonic motions in the high-β plasmas considered here; however, the closure is useful for comparison with the LF closure by virtue of its relative simplicity. It has also been employed in a variety of previous computational studies (e.g. S06; Kowal, Falceta-Gonçalves & Lazarian 2011, Santos-Lima *et al.* 2014), and so it is worthwhile to diagnose the model's successes and limitations.

An important caveat for each of these approximations to (2.4)–(2.5) relates to plasma microinstabilities. For our purposes, given the focus of this work on the high-β regime, the most significant of these are the firehose instability (Rosenbluth 1956; Chandrasekhar, Kaufman & Watson 1958; Parker 1958; Yoon, Wu & de Assis 1993), which is excited if

$$\Delta \lesssim -\frac{2}{\beta}, \tag{2.9}$$

and the mirror instability (Hasegawa 1969; Southwood & Kivelson 1993; Hellinger 2007), which is excited if

$$\Delta \gtrsim \frac{1}{\beta}. \tag{2.10}$$

(There are corrections to these β-dependent thresholds that arise from particle resonances and depend on the specific form of the distribution function; see, e.g. Klein & Howes 2015.) Important aspects of these instabilities (e.g. their regularization at small scales or particle scattering in their nonlinear evolution) are not captured by the closures we employ here, and kinetic calculations are needed to correctly understand their saturation. There have been a variety of recent works in this vein (Hellinger & Trávníček 2008; Schekochihin *et al.* 2008; Rosin *et al.* 2011; Kunz, Schekochihin & Stone 2014*a*; Hellinger *et al.* 2015; Rincon, Schekochihin & Cowley 2015; Riquelme, Quataert & Verscharen 2015; Sironi & Narayan 2015; Melville, Schekochihin & Kunz 2016; Riquelme, Quataert & Verscharen 2016), which have shown that these microinstabilities generally act to pin the pressure anisotropy at the marginal stability limits. Interestingly, when Δ is driven beyond the stability boundaries, the microinstabilities achieve this in two stages: first, while the microscale fluctuations are growing secularly, by increasing (if $d_t B < 0$) or decreasing (if $d_t B > 0$) the magnetic-field strength B (in other words, the small-scale fluctuations contribute to B); second, as the instabilities saturate, by enhancing the scattering of particles and thus increasing ν_c in (2.4)–(2.5). While the time for the firehose instability at moderate β to saturate is essentially set by gyro-scale physics, and so might be

considered as instantaneous in a fluid model, the mirror instability saturates on a time scales comparable to the turnover time of the large-scale motions driving the anisotropy (see § 6.3 and Kunz *et al.* 2014*a*, Rincon *et al.* 2015, Riquelme *et al.* 2015, Melville *et al.* 2016). We also note that there are also various other kinetic instabilities that could be important, for instance, the ion-cyclotron instability, or electron instabilities. We do not consider these in detail because the mirror and firehose instabilities are thought to be the most relevant to the high-β, ion-dominated regime that is the focus of this work (see § 5 for further discussion).

In practice, because the primary effect in both the secular and scattering regimes is to limit Δ at the threshold boundaries, we model these effects as a 'hard-wall' limit on Δ, following prior work (S06; Sharma *et al.* 2007, Santos-Lima *et al.* 2014, Chandra *et al.* 2015, Foucart *et al.* 2015). This simply limits Δ to $1/\beta$ or $-2/\beta$ if the dynamics drives Δ across these boundaries.[3] One should, however, be careful with this simple 'limiter' method not to inadvertently remove interesting physics from the model. For instance, the parallel firehose instability is destabilized at the same point $\Delta = -2/\beta$ as where the magnetic tension is nullified by Δp (indeed, this is the cause of the instability), which can have a strong influence on the largest scales (Squire, Quataert & Schekochihin 2016; Squire *et al.* 2017) and is captured in even our simplest 1-D models. For this reason, in considering azimuthal-field KMRI modes, we have run calculations both with and without a firehose limiter, seeing very similar dynamics in each case. Finally, we note that with finite scale separations between Ω_i and S, as is the case in numerical simulations (Riquelme *et al.* 2012; Hoshino 2015; Kunz *et al.* 2016), there can be significant overshoot of the pressure anisotropy beyond the limits (2.9) and (2.10) (Kunz *et al.* 2014*a*). This overshoot may be important for the large-scale evolution (see § 3) but is probably not representative of what happens in real systems, which usually have a very large dynamic range between Ω_i and S. These effects are discussed in detail in § 6.

2.2. *Computational methods*

A number of different numerical methods are used to solve (2.1)–(2.7). For investigating the 1-D evolution of a channel mode, we use a pseudo-spectral method, with standard dealiasing and hyper-diffusion operators used to remove the energy just above the grid scale. A very similar numerical method, albeit on a 3-D Fourier grid, is used for the studies of parasitic modes. For studies of the fully nonlinear 3-D evolution, we use a modified version of the finite-difference code ZEUS, as described in S06. For simulations in the weakly collisional regime, we solve the full LF system (2.1)–(2.7), so as to correctly capture the effects of the heat fluxes in the moderate- and high-collisionality regimes (see § B.4).

A few words are needed regarding the numerical treatment of heat fluxes in the LF model (2.6)–(2.7). In particular, the $1/|k_\parallel|$ operator is numerically awkward, because it is not diagonal in either Fourier space or real space. We thus use the prescription of S06 and replace this by a pre-chosen k_L for the ZEUS implementation and the parasitic-mode studies, while for the 1-D collisionless calculations we use $1/|k_\parallel| = 1/|k_z|$ (once the mode reaches larger amplitude this may somewhat underestimate the heat fluxes,

---

[3]Within the context of the LF closure (2.1)–(2.7), the only obvious place where the difference between saturation via unresolved small-scale fields and saturation via particle scattering may be important is in the heat fluxes. These are significantly reduced at high collisionality (see (2.6) and (2.7)), and likely also modified by microscale mirror or firehose fluctuations (Komarov *et al.* 2016; Riquelme *et al.* 2016; Riquelme, Quataert & Verscharen 2017). We have experimented with either including ν_c in $q_{\perp,\parallel}$ at the mirror and firehose boundaries or not, and this difference does not appear to strongly affect the results presented herein.

since $k_\parallel < k_z$ if the field lines are not straight). Following S06, we have checked that varying the choice of k_L within a reasonable range, or using the choice $|k_\parallel| = |k_z|$, does not significantly affect the dynamics.

We use the methods detailed in appendix A3 of S06 to limit the pressure anisotropy: ν_c is instantaneously increased in (2.4)–(2.5) whenever Δ passes the limits (2.9) or (2.10). We do not make any distinction between the 'secular growth' and 'particle scattering' phases of microinstability evolution with this method (see discussion above, around (2.10), and § 6.3), and more study is needed to better understand the successes and limitations of this simple limiter approach.

2.3. *General comparison of kinetic models*

Before commencing with our analysis of the KMRI, we highlight in this section some of the key similarities and differences between the LF, Braginskii and CGL models, as well as that of standard MHD.

First, irrespective of the closure details, the general effect of pressure anisotropy is to modify the Lorentz force, either by enhancing ($\Delta p > 0$) or reducing ($\Delta p < 0$) the effective magnetic tension (see (2.2)). The same relative pressure anisotropy $\Delta = \Delta p / p_0$ will thus have a greater dynamical effect as β increases, because p_0 increases compared to B. In contrast, the generation of Δ in a changing magnetic field,

$$\frac{\mathrm{d}\Delta}{\mathrm{d}t} \sim \hat{\boldsymbol{b}}\hat{\boldsymbol{b}} : \nabla \boldsymbol{u} \sim \frac{\mathrm{d}\ln B}{\mathrm{d}t} \tag{2.11}$$

(or $\Delta \sim \nu_c^{-1}\hat{\boldsymbol{b}}\hat{\boldsymbol{b}} : \nabla \boldsymbol{u}$ for Braginskii), does not depend on β. Thus, the dynamics of higher-β plasmas is in general more strongly influenced by self-generated pressure anisotropies than is the dynamics of lower-β plasmas.

Secondly, the spatial form of Δp generated in a given time-dependent B differs significantly between the LF, CGL and Braginskii models. This Δp is important for the nonlinear behaviour of the collisionless MRI. The influence of a spatially constant Δ can be considered from an essentially linear standpoint: it simply acts to enhance or reduce the Lorentz force by the factor $(1 + \beta\Delta/2)$. In contrast, when the spatial variation in Δ is similar to its magnitude, its effect is inherently nonlinear. For the same reason, detailed conclusions about the expected change in the spatial shape of an MRI mode due to pressure anisotropy do depend on the regime of interest (and model) – for example, collisionless versus Braginskii (Squire *et al.* 2016), or low versus high β – rather than being generic consequences of any self-generated pressure anisotropy. For our purposes, one can consider high-collisionality Braginskii MHD (equation (2.8)) as the limiting model that develops large spatial variation in Δ (since Δ is tied directly to $\mathrm{d}_t B$), while the high-β limit of the LF model is the opposite, developing large Δ with very little spatial variation.[4] This is because collisions generically act to reduce the magnitude of Δ without affecting the spatial variation in $p_\perp$ and $p_\parallel$, whereas heat fluxes act to reduce spatial variation in $p_\perp$ and $p_\parallel$ without affecting the spatial average of Δ.

This last statement warrants further explanation, given the complexity of (2.4)–(2.7). The effect of the LF heat fluxes (2.6)–(2.7) can be clarified if we assume $\nu_c = 0$ and $\Delta p \ll p_0$ (the latter is always valid at high β), so that

$$q_\parallel \approx -\sqrt{\frac{8}{\pi}}\rho c_s \frac{\nabla_\parallel}{|k_\parallel|}\left(\frac{p_\parallel}{\rho}\right), \quad q_\perp \approx -\sqrt{\frac{2}{\pi}}\rho c_s \frac{\nabla_\parallel}{|k_\parallel|}\left(\frac{p_\perp}{\rho}\right). \tag{2.12a,b}$$

---

[4]The double-adiabatic model and moderate-collisionality Braginskii regime lie somewhere between these limits; see (B 12).

Then, assuming $\hat{\boldsymbol{b}} \cdot \nabla q_{\perp,\parallel} \gg q_{\perp,\parallel} \nabla \cdot \hat{\boldsymbol{b}}$, which is valid when the perturbation to the background field is small (i.e. when the field lines are nearly straight), the contribution to the $p_\perp$ and $p_\parallel$ evolution equations has the form $\partial_t p_\perp \sim -\rho c_s |k_\parallel|(p_\perp/\rho)$ and $\partial_t p_\parallel \sim -\rho c_s |k_\parallel|(p_\parallel/\rho)$, respectively. These terms, which model the effect of Landau damping (Snyder *et al.* 1997), act as a 'scale-independent' diffusion of $p_\perp$ and $p_\parallel$, damping inhomogeneities[5] over the sound-wave time scale $|k_\parallel|c_s$. This is important because $|k_\parallel|c_s \sim \beta^{1/2}\gamma_{\mathrm{MRI}}$ (where γ_{MRI} is the MRI growth rate), showing that for $\beta \gg 1$, the heat fluxes will rapidly erase spatial variation in Δp on the time scale that the MRI grows. As a result, the spatial variation in Δp will be dwarfed by its mean; i.e. Δp will be nearly spatially constant. A more thorough discussion of these ideas is given in appendix B, where we solve explicitly for the Δp that arises in an exponentially growing, spatially varying magnetic perturbation. This shows that the double-adiabatic model for $p_{\perp,\parallel}$ generates a Δp with spatial variation of the order of its mean, while the addition of LF heat fluxes decreases the spatial variation of Δp by a factor $\beta^{1/2}$ while leaving the mean Δp unchanged.

3. One-dimensional evolution

In this section, we discuss various nonlinear effects that occur due to the pressure anisotropy that develops in a growing KMRI mode. These effects are one-dimensional (i.e. unrelated to 'parasitic' modes and turbulence, which is discussed in §4) and occur at very low mode amplitudes: when $\delta B \sim \beta^{-1/2}B_0$ in a purely vertical field, or when $\delta B_y \sim \beta^{-2/3}B_0$ and $\delta B_x \sim \beta^{-1/3}B_0$ with an azimuthal field (where δB denotes the mode amplitude). This provides an interesting counterpoint to MHD MRI channel modes, which are nonlinear solutions of the incompressible MHD equations (Goodman & Xu 1994), and only exhibit notable nonlinear modifications as the mode amplitude approaches the sound speed, $\delta B \sim \beta^{1/2}B_0$. However, we will also see that despite this early (low-amplitude) nonlinear modification, once a KMRI mode's amplitude starts to dominate over the background field ($\delta B \gtrsim B_0$), it reverts to being an approximate nonlinear solution, because of the pressure-anisotropy-limiting behaviour of the mirror instability. Thus a KMRI mode behaves very similarly to an MHD channel mode as δB approaches $\beta^{1/2}B_0$.

We begin by outlining the basic linear physics of the KMRI (§3.1), which will be relevant to its nonlinear evolution. We then examine various stages in the evolution of a 1-D collisionless KMRI mode in vertical (§3.2) or mixed-azimuthal–vertical (§3.3) background magnetic fields, before the mode saturates into turbulence. We also discuss how these stages are modified in the weakly collisional (Braginskii) regime (§§3.2.2, 3.3.2). Throughout this section we denote the MRI perturbation velocity and magnetic field as $\delta \boldsymbol{u}$ and $\delta \boldsymbol{B}$ respectively (their magnitudes are δu and δB), the background magnetic field as $\boldsymbol{B}_0 = B_{0y}\hat{\boldsymbol{y}} + B_{0z}\hat{\boldsymbol{z}}$, and $\beta_0 = 8\pi p_0/B_0^2$ is defined with respect to the background field (we also use $\beta_{0z} = 8\pi p_0/B_{0z}^2$). For the reader interested in a general overview of results, the summary in §3.4 should be understandable without a careful reading of §§3.1–3.3.

---

[5]The heat-flux-induced damping is technically of $p_\perp/\rho = T_\perp$ and $p_\parallel/\rho = T_\parallel$, rather than of $p_\perp$ and $p_\parallel$ themselves. Because the spatial variation in ρ will generally be similar to that of $p_{\perp,\parallel}$, the effective damping is less than what it would be if the variation in ρ were ignored (see §B.3, equations (B 22)–(B 23)). However, this variation in ρ can never completely cancel the variation in $p_{\perp,\parallel}$ and preclude damping: there is always some $T_{\perp,\parallel}$ variation induced by the changing magnetic-field strength.
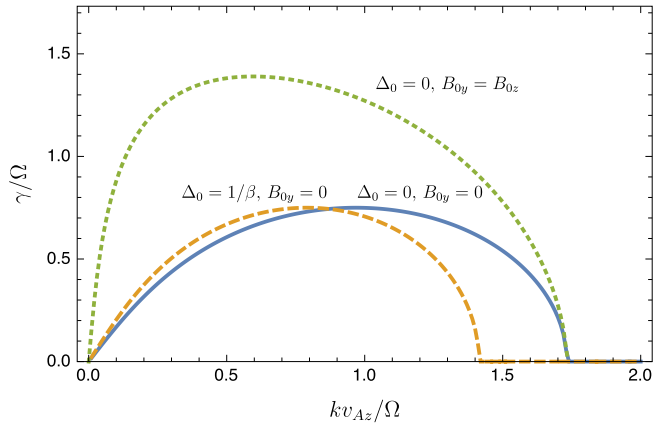
FIGURE 1. Dimensionless linear growth rate γ/Ω of the KMRI at $\beta_{0z} = 8\pi p_0/B_{0z}^2 = 400$ and $S/\Omega = 3/2$, plotted as a function of dimensionless vertical wavenumber $k_z v_{Az}/\Omega$ (with $k_x = k_y = 0$). The solid blue curve shows the case with a purely vertical $\boldsymbol{B}_0$ and no background pressure anisotropy Δ_0, for which the dispersion relation is identical to the standard MRI. The orange dashed line shows the case with $B_{0y} = 0$ and $\Delta_0 = 1/\beta_0$, which is approximately the anisotropy at which the mirror limit is first reached in the growing mode. Finally, the green dotted line shows the growth rate in the case with an azimuthal field $B_{0y} = B_{0z}$ (with $\beta_{0z} = 400$, $\beta_0 = 200$), where the growth rate is strongly enhanced compared to the MHD MRI (which is unaffected by the azimuthal field for $k_x = k_y = 0$).

3.1. *Linear KMRI*

Before discussing any nonlinear effects, it is helpful to first review aspects of the linear KMRI. We consider only the simplest case of purely vertical wavenumbers $k_z \neq 0$, $k_x = k_y = 0$; i.e. ($\boldsymbol{k} \parallel \boldsymbol{B} \parallel \boldsymbol{\Omega}$). This choice is motivated by the stabilizing influence of a non-zero radial wavenumber k_x (see discussion in §4 of Q02), meaning that $k_x = 0$ modes should dominate if growing from small amplitudes, while treating $k_y \neq 0$ modes requires a global and/or time-dependent method (Balbus & Hawley 1992; Johnson 2007; Squire & Bhattacharjee 2014*a*). We also neglect the possibility of a radial background magnetic field since this leads to a time-dependent background azimuthal field. More thorough discussion and detailed derivations can be found in Q02; Sharma *et al.* (2003), Balbus (2004), Rosin & Mestel (2012), Heinemann & Quataert (2014), Quataert *et al.* (2015), as well in appendix A, where we derive properties of the KMRI in a mixed-vertical–azimuthal field.

We linearize (2.1)–(2.7) with $\nu_c = 0$ and $S/\Omega = 3/2$, then insert the Fourier ansatz $\delta f(z, t) = \delta f \mathrm{e}^{\mathrm{i}kz - \mathrm{i}\omega t}$ for each variable ($f = \rho$, $\boldsymbol{u}$, $\boldsymbol{B}$ etc.). Solution of the resulting polynomial equation for ω yields the linear KMRI growth rates, $\gamma/\Omega = \mathrm{Im}(\omega)/\Omega$, as shown in figure 1 for several relevant cases. For the case of purely vertical field and no background pressure anisotropy (solid line), the KMRI dispersion relation is identical to the collisional MRI. This occurs because when $\boldsymbol{B}_0 = B_0\hat{\boldsymbol{z}}$ the MRI does not linearly perturb the pressure (because $\partial_z(\boldsymbol{B}_0 \cdot \delta\boldsymbol{B}) = 0$), and thus is ignorant of the equation of state. With a non-zero radial wavenumber $k_x \neq 0$, this is no longer the case (since then $\delta B_z \neq 0$), and the growth rate is lower than for the standard MRI.

The addition of a background positive pressure anisotropy, $\Delta_0 > 0$, shifts the MRI to larger wavelengths (smaller k; dashed curve in figure 1). This is because the anisotropic-pressure stress in the momentum equation has a form identical to that of

the Lorentz force (see (2.2)). Thus the only difference in comparison to the standard MRI dispersion relation is the replacement of $k v_A$ with $k v_A (1 + \beta_0 \Delta_0/2)^{1/2}$, which decreases the wavenumber that maximizes γ from $\sim \Omega v_A^{-1}$ to $\sim \Omega v_A^{-1}(1 + \beta_0 \Delta_0/2)^{-1/2}$, while keeping the maximum itself constant. This is relevant to the nonlinear behaviour of the KMRI, since the mode generates a pressure anisotropy as it evolves.

Finally, the addition of a background azimuthal field causes the KMRI dispersion relation to differ significantly from that of the standard MRI (Q02; Balbus 2004; dotted curve in figure 1), increasing the growth rate and moving the instability to larger wavelengths. This differs from the standard (MHD) MRI, which is unaffected by $B_{0y} \neq 0$ when $k_y = 0$. Due to the different physical processes that lead to the large growth rates at low k, this instability is also known as the magnetoviscous instability (MVI; Balbus 2004). Unlike the standard MRI, the growth mechanism relies on the azimuthal pressure force $\hat{\boldsymbol{b}}_0 \hat{\boldsymbol{b}}_0 \delta \Delta p$, which is destabilizing and dominates over the magnetic tension by a factor of $\beta_0^{1/2}$ (see Q02). As shown in appendix A, for $\beta_0 \gg 1$ the KMRI growth rate approaches $\gamma = (2S\Omega)^{1/2}$, with a maximum growth rate at wavenumber $k_{\max} v_{Az}/\Omega \approx 1.8\,\beta_{0z}^{-1/6}$ when $B_{0y} \approx B_{0z}$ and $S/\Omega = 3/2$ (see (A 2)). In this fastest-growing mode, the relative amplitudes of the various components are $\beta_0^{-2/3} \delta B_x/B_0 \sim \beta_0^{-1/3} \delta B_y/B_0 \sim \beta_0^{-5/6} \delta u_x/v_A \sim \beta_0^{-5/6} \delta u_y/v_A \sim \delta p_{\perp,\parallel}/p_0$ (unlike the standard MRI, where $\delta B_x/B_0 \sim \delta B_y/B_0 \sim \delta u_x/v_A \sim \delta u_y/v_A$). While we shall use these scalings below in our discussion of the nonlinear behaviour of MRI modes, we caution that they only apply at rather high β_0, a problem that is exacerbated if $B_{0y}/B_{0z} \neq 1$. At more moderate β_0, as feasible for simulations, $k_{\max}$ tends towards its value for the standard MRI, $k_{\max} v_{Az}/\Omega \approx 1$ (see figure 7). It is also worth noting that the dispersion relation, $\gamma(k)$, varies only slowly around $k = k_{\max}$ (see e.g. dotted curve in figure 1). This implies that, if starting from random initial conditions, a long time would be required before the fastest-growing mode dominates, suggesting that when nonlinear effects become important there will likely still be several modes of similar amplitudes. With these caveats duly noted, in our discussion of nonlinear effects below (§ 3.3), we will consider only the fastest-growing KMRI mode (i.e. set $k = k_{\max}$) and use the above scalings, rather than keep k arbitrary.

3.2. *Nonlinear KMRI: vertical magnetic field*

In this section, we consider the nonlinear evolution of the MRI in a vertical background field. In this case the linear dispersion relation is identical to that obtained in ideal MHD. However, we shall show that the modes are (modestly) nonlinearly modified by the pressure anisotropy at low amplitudes $\delta B \sim \beta^{-1/2} B_0$. To do so, we first describe the evolution of a truly collisionless mode using the LF closure with $\nu_c = 0$ (§ 3.2.1), and then examine the weakly collisional Braginskii case in § 3.2.2.

3.2.1. *Collisionless (LF) regime*

A maximally unstable MRI mode satisfies

$$\delta u_x = \delta u_y = -\sqrt{\frac{3}{5}} \frac{\delta B_0}{\sqrt{4\pi\rho}} \mathrm{e}^{\gamma t} \sin(kz), \tag{3.1a}$$

$$-\delta B_x = \delta B_y = \delta B_0 \mathrm{e}^{\gamma t} \cos(kz), \tag{3.1b}$$

where $\gamma = S/2$ is the growth rate and δB_0 is the initial mode amplitude. Because of the opposing signs between $\delta B_x \delta u_x$ and $\delta B_y \delta u_y$ in the mode, only $-S\hat{b}_x \hat{b}_y$ contributes
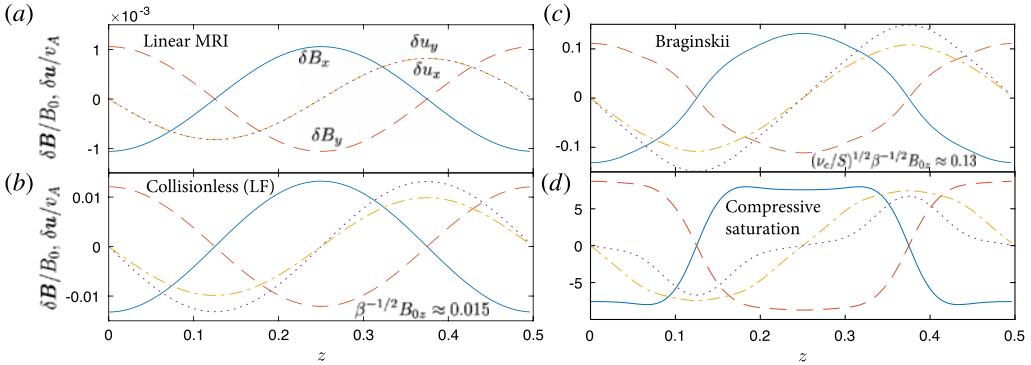
FIGURE 2. The structure of a kinetic MRI mode evolving in a vertical background field B_{0z} in various regimes, as computed from the 1-D LF model (with $\nu_c \neq 0$ in panel c). We take $\beta_0 = 337$ in a domain with $\Omega L_z/c_s = 1$, such that the peak of the MRI dispersion relation (i.e. the maximum γ) is at $k = 2 \times 2\pi/L_z$ (each panel shows only half of a scale height). Each plot illustrates δB_x (blue solid line), δB_y (red dashed line), δu_x (yellow dot-dashed line) and δu_y (purple dotted line). The various panels show: (a) the linear KMRI mode (this is the initial conditions for each simulation), which is identical in structure to an MHD MRI mode at these parameters; (b) the collisionless MRI mode when Δp reaches the mirror limit ($\delta B \sim \beta^{-1/2} B_{0z} \approx 0.015$), which remains very nearly sinusoidal because the heat fluxes make Δp spatially uniform; (c) a mode in the high-collisionality Braginskii regime (with $\nu_c/S = \beta_0^{3/4}$) when Δp reaches the mirror limit (at $\delta B \sim (\nu_c/S)^{1/2}\beta^{-1/2}B_{0z} \approx 0.13$), which is non-sinusoidal because of the $O(1)$ spatial variation in Δp; (d) the MRI mode at very large amplitudes, when compressibility becomes important. The structure of this final compressible stage of evolution is the same across all models, including standard (collisional) MHD.

to $\hat{b}\hat{b} : \nabla u \approx -S\delta B_x \delta B_y / B_{0z}^2$. As shown in § B.3, at high β in a collisionless plasma (using the LF closure), the mean of the pressure anisotropy dominates over its spatial variation by a factor of $\beta^{1/2}$ (see (B 21)–(B 24)), and Δ is approximately spatially constant:

$$\Delta \sim \frac{3}{2}\frac{\delta B_0^2}{B_{0z}^2}\mathrm{e}^{2\gamma t}. \tag{3.2}$$

The mirror threshold is reached at $\Delta = 1/\beta$, when $\delta B/B_{0z} \sim \beta_0^{-1/2}$. As discussed in § 3.1, a positive pressure anisotropy modifies the MRI mode by effectively increasing the magnetic tension, and the mode will be stabilized if $kv_A\sqrt{1 + \Delta(t)\beta_0/2} \geqslant \sqrt{2S\Omega}$. Fortunately, for a mode near the peak growth rate, $kv_A = \sqrt{S(\Omega - S/4)}$, this stabilization does not occur, because the fast-growing mirror fluctuations limit $\sqrt{1 + \Delta(t)\beta_0/2}$ to values at or below $\sqrt{3/2}$. As shown in figure 2(b), this pressure anisotropy causes a rather minor modification to the shape of the MRI mode because Δp is almost spatially constant, decreasing u_x and B_y relative to u_y and B_x in the same way as for an MHD MRI mode that is not at the fastest-growing wavelength.[6]

---

[6]Note that if there is insufficient scale separation between the gyrofrequency and the MRI growth rate, the pressure anisotropy may grow far enough beyond the mirror limit to stabilize the mode, which occurs if $\Delta \geqslant 2\beta_0^{-1}[2S\Omega/(kv_A)^2 - 1]$. In this case, the mode can move to longer wavelengths and continue to grow if there is sufficient space in the box. This occurs in the simulations of S06, where the chosen mirror limit 'hard wall' is $\Delta = 3.5/\beta$, large enough that pressure anisotropy would stabilize the fastest-growing MRI mode before Δ is artificially limited; see §§ 4 and 6 for further discussion.

As the mode continues to evolve to larger amplitudes $\delta B/B_{0z} \gtrsim \beta_0^{-1/2}$, the pressure anisotropy remains limited by mirror fluctuations. Leaving aside, for the moment, questions related to how the mode disrupts and becomes turbulent, there are two other amplitudes of interest: (i) when the mode amplitude surpasses the background field at $\delta B/B_{0z} \sim 1$, and (ii) when compressibility becomes important at $\delta B/B_{0z} \sim \beta_0^{1/2}$ ($\delta u \sim c_s$). Interestingly, if the pressure anisotropy is efficiently limited by mirror fluctuations, $\Delta p = B^2/8\pi$, then the pressure anisotropy nonlinearity has little effect:

$$\nabla \cdot (\Delta p \hat{\boldsymbol{b}}\hat{\boldsymbol{b}}) = \frac{\nabla \cdot (B^2 \hat{\boldsymbol{b}}\hat{\boldsymbol{b}})}{8\pi} = \frac{\boldsymbol{B} \cdot \nabla \boldsymbol{B}}{8\pi} = \frac{\boldsymbol{B}_0 \cdot \nabla \delta \boldsymbol{B} + \delta \boldsymbol{B} \cdot \nabla \delta \boldsymbol{B}}{8\pi} = \frac{\boldsymbol{B}_0 \cdot \nabla \delta \boldsymbol{B}}{8\pi}, \qquad (3.3)$$

since $\delta \boldsymbol{B} \cdot \nabla \delta \boldsymbol{B} \approx 0$ for an MRI channel mode (Goodman & Xu 1994). Thus, once $\delta B_x \sim \delta B_y \gtrsim B_0$, the effect of the pressure-anisotropy nonlinearity on the mode remains identical to when $\delta B_x \sim \delta B_y \lesssim B_0$, even though the pressure anisotropy has a large ($\Delta p \sim \delta B^2$) variation in space (i.e. the change is simply a modified magnetic tension, as shown in figure 2b). In other words, because $\Delta p \propto B^2$, there is no significant change to the mode as the mode amplitude surpasses the background field strength.

The final phase of evolution, once $\delta B \sim \beta^{1/2} B_0$ (i.e. $\delta u \sim c_s$), is then very similar to standard MHD, and the mode develops a rather distinctive shape, which we illustrate in figure 2(d). Because the nonlinearity is dominated at this point in the evolution by inhomogeneities in the density, this mode shape appears generically in all of the models studied here (including compressible MHD) across a wide range of parameters (cf. Latter *et al.* 2009).

3.2.2. *Weakly collisional (Braginskii) regime*

In the Braginskii regime, which is valid for $\bar{\nu}_c \equiv \nu_c/S \sim \nu_c/\gamma \gg 1$ and is relevant (i.e. represents a potentially significant correction to standard MHD) when $\bar{\nu}_c \ll \beta_0$, there are two subregimes. In the moderate-collisionality regime, $\bar{\nu}_c \ll \beta_0^{1/2}$, the heat fluxes play a very significant role and smooth the pressure anisotropy spatially, as occurs in the collisionless case described in § 3.2.1. In the high-collisionality regime, $\bar{\nu}_c \gg \beta_0^{1/2}$, the heat fluxes are sub-dominant and do not play a significant dynamical role, leading to Δp profiles that vary significantly in space. For more information, see § B.4 and appendix B of Squire *et al.* (2017).

In the moderate-collisionality regime, up to $\bar{\nu}_c \lesssim \beta_0^{1/2}$, the behaviour of the mode at amplitudes $\delta B \lesssim (\beta_0/\bar{\nu}_c)^{1/2} B_0$ (see below) is effectively identical to the collisionless regime discussed in § 3.2.1. In particular, the pressure anisotropy that develops from the growing mode with $\delta B \ll B_0$ is

$$\Delta \approx \frac{1}{\nu_c} \langle \hat{\boldsymbol{b}}\hat{\boldsymbol{b}} : \nabla \boldsymbol{u} \rangle \sim \frac{S}{\nu_c} \frac{\delta B_0^2}{B_{0z}^2} e^{2\gamma t} = \frac{1}{\bar{\nu}_c} \frac{\delta B_0^2}{B_{0z}^2} e^{2\gamma t}, \qquad (3.4)$$

because the heat fluxes are smoothing Δp faster than it is being created (by some factor between $\beta_0^{1/2}$ and 1, depending on $\bar{\nu}_c \beta_0^{-1/2}$; see Squire *et al.* 2017). Thus, by the time that Δp reaches the mirror limit (i.e. when $\delta B \sim (\bar{\nu}_c/\beta_0)^{1/2} B_0$), it is nearly smooth in space, implying that the same conclusions reached in the collisionless limit also apply here. The same is then true as the mode continues growing to $\delta B \gtrsim B_0$ (but $\delta B \lesssim (\beta_0/\bar{\nu}_c)^{1/2} B_0$); it forces Δp to the mirror limit everywhere in space, implying the mode is not strongly affected by the pressure-anisotropy nonlinearity (see (3.3)).

In the high-collisionality regime, $\bar{\nu}_c \gg \beta_0^{1/2}$, the heat fluxes do not significantly smooth spatial variation in Δp and we must modify various aspects of the conclusions

from the previous section. The pressure anisotropy that develops from the growing mode (for $\delta B \ll B_0$) is now spatially inhomogeneous:

$$\Delta = \frac{1}{\nu_c} \hat{\boldsymbol{b}}\hat{\boldsymbol{b}} : \nabla \boldsymbol{u} \sim \frac{1}{\overline{\nu}_c} \frac{\delta B_0^2}{B_{0z}^2} \, \mathrm{e}^{2\gamma t} \cos^2(kz). \tag{3.5}$$

This implies that, as the pressure anisotropy first reaches the mirror limit in some regions of space (near the antinodes of the mode, where $\mathrm{d}_t \ln B$ is largest), it also changes the shape of the mode, *viz.*, it couples different Fourier components of $\delta \boldsymbol{B}$ and $\delta \boldsymbol{u}$. This causes minor modifications to the shape of the mode, which are shown in figure 2(c) for $\overline{\nu}_c = \beta_0^{3/4}$ (i.e. in the middle of the high-collisionality regime; the shape changes at other $\overline{\nu}_c$ and β_0 are generally similar to this). As the mode grows further, Δp becomes limited by the mirror instability ($\Delta p \propto B_0^2 + \delta B^2$) across a larger region of space, implying (by the arguments above) that the mode regains its sinusoidal shape (albeit briefly, see next paragraph).

There is one final effect, not included in the collisionless discussion, which occurs in both the moderate-collisionality and high-collisionality Braginskii regimes at large mode amplitudes, $\delta B \gtrsim (\beta_0/\overline{\nu}_c)^{1/2} B_0$. The difference compared to the collisionless case arises because, in the Braginskii regime, Δp is proportional to the current value of $\hat{\boldsymbol{b}}\hat{\boldsymbol{b}} : \nabla \boldsymbol{u}$ rather than to its time history. Once $\delta B \gtrsim B_0$, this value $\hat{\boldsymbol{b}}\hat{\boldsymbol{b}} : \nabla \boldsymbol{u} \approx -S\delta B_x \delta B_y / \delta B^2$ becomes constant in time, despite the fact that $B^2 \approx \delta B^2$ is growing. Thus, Δp moves back below the mirror limit when $\delta B^2 \gtrsim p_0/\overline{\nu}_c$, *viz.*, when $\delta B \gtrsim (\beta_0/\overline{\nu}_c)^{1/2} B_0$. This occurs before compressibility affects the mode (at $\delta B \sim \beta_0^{1/2} B_0$), and causes the pressure anisotropy to vary in space, which in turn modifies the shape of the mode. These modifications are very minor, even at very high $\beta_0 \sim 10^5$ and high $\overline{\nu}_c$ (not shown), and so it seems unlikely that they should modify mode saturation in three dimensions in any significant way. As the amplitude approaches $\delta B \sim \beta_0^{1/2} B_0$, the mode is affected by compressibility in exactly the same way as is the collisionless (or MHD) MRI (see figure 2d).

3.3. *Nonlinear KMRI: azimuthal–vertical magnetic field*

In this section, we consider the effect of an additional background azimuthal magnetic field. We focus mainly on the collisionless KMRI (LF model; § 3.3.1), briefly mentioning the Braginskii version (for which the conclusions are similar) in § 3.3.2. As shown in figure 1, the MRI (or MVI) under such conditions is significantly different from the vertical background field case, growing fastest at long wavelengths $k_{\max} v_{Az}/\Omega \ll 1$ with growth rates exceeding $S/2$. This situation is arguably more relevant astrophysically than is the pure vertical-field case: at high β_0, even small azimuthal fields significantly modify the dispersion relation (see appendix A).

3.3.1. *Collisionless (LF) regime*

As with the vertical-field KMRI, nonlinear effects become important in the collisionless case at very low amplitudes, specifically when $\delta B_y \sim \beta_0^{-2/3} B_0$ (or when $\delta B_x \sim \beta_0^{-1/3} B_0$, see (A 4)–(A 7)). Once the perturbed field becomes larger than the background field, the magnetic field is dominated by the mode itself and the instability again becomes similar to the MHD MRI (or, equivalently, the vertical-field KMRI at large amplitudes).
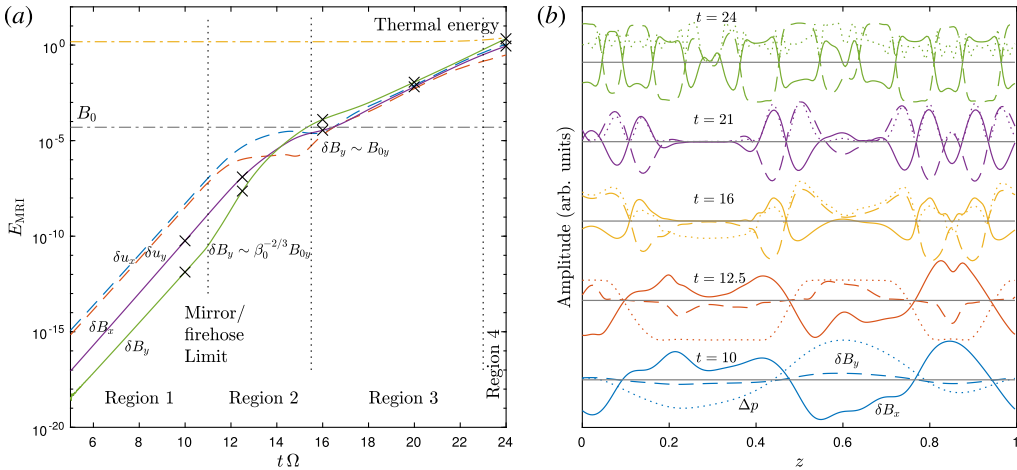
FIGURE 3. (*a*) Energy evolution of each component of the growing KMRI mode in a mixed-azimuthal–vertical field with $B_{0y} = B_{0z}$, at $\beta_0 = 5000$ ($\beta_{0z} = 10\,000$) in a domain such that $\Omega L_z/c_s = 1$. We show δB_x (solid purple line; $E_{\mathrm{MRI}} = \int \mathrm{d}z\, \delta B_x^2/8\pi$), δB_y (solid green line; $E_{\mathrm{MRI}} = \int \mathrm{d}z\, \delta B_y^2/8\pi$), δu_x (dashed blue line; $E_{\mathrm{MRI}} = \int \mathrm{d}z\, \rho \delta u_x^2/2$), and δu_y (dashed red line; $E_{\mathrm{MRI}} = \int \mathrm{d}z\, \rho \delta u_y^2/2$). The calculation, which uses the 1-D LF model (2.1)–(2.7) with $\nu_c = 0$, is initialized with random Fourier amplitudes, scaled by k^{-2} (initial phase of evolution not shown for clarity). For comparison, we also show the thermal energy (yellow dot-dashed line) and the energy of the background magnetic field (grey dot-dashed line). Following the linear phase with large growth rate (Region 1), the linearly perturbed pressure anisotropy reaches the mirror and firehose limits when $\delta B_y \sim \beta_0^{-2/3} B_{0y}$, $\delta B_x \sim \beta_0^{-1/3} B_{0y}$. There follows a transition phase (Region 2) in which the perturbed pressure anisotropy can no longer contribute to the instability and the mode moves to the much shorter wavelengths characteristic of the standard MRI. Then, once $\delta B_y > B_{0y}$, the mode grows similarly to the vertical-field KMRI (Region 3) with Δ at the mirror limit, until finally it is affected by compressibility in the same way as illustrated in figure 2(*d*) (Region 4). (*b*) Spatial structure of the azimuthal-field KMRI mode at a variety of times corresponding to '×' markers in panel (*a*), which are chosen to illustrate the different phases of evolution. At each time, offset on the vertical axis for clarity with times listed in units of Ω^{-1}, we show $\delta B_x/\max(\delta B)$ with solid lines, $\delta B_y/\max(\delta B)$ with dashed lines, and $\Delta p/\max(|\Delta p|)$ with dotted lines (the grey lines show 0 to more clearly separate each curve). The mode transitions (around $t \approx 16\, \Omega^{-1}$) from structures characteristic of the azimuthal-field KMRI with Δp both positive and negative, to those characteristic of the MHD-like vertical-field MRI, with the pressure anisotropy everywhere positive and at the mirror limit. Although less clean than the single-mode case studied in figure 2, the structures at very late times ($t = 24$) are again affected by compressibility in the same way (cf., δB_x and δB_y with those shown in figure 2*d*).

We now describe how such a mode transitions through four distinct stages in its nonlinear evolution, which is illustrated schematically in figure 3. Let us consider each stage of evolution separately, assuming $B_{0y} \approx B_{0z} = B_0/\sqrt{2}$ for the sake of simplicity:

(1) *Linear evolution.* Unlike in the vertical-field case, the KMRI mode linearly produces a pressure anisotropy,

$$\Delta \approx \sqrt{2\pi}\, \frac{1}{c_s k}\, \frac{\partial_t \delta B_y}{B_0} \approx \sqrt{2\pi}\, \frac{\gamma}{c_s k}\, \frac{\delta B_y}{B_0}, \tag{3.6}$$

because $\delta\boldsymbol{B}\cdot\boldsymbol{B}_0 = \delta B_y B_{0y} \neq 0$ (here we have set $B_{0y} \approx B_{0z}$; see Q02 and appendix A). This implies that, as the mode evolves, it pushes the plasma towards both the mirror limit, in regions where $\delta\boldsymbol{B}\cdot\boldsymbol{B}_0 > 0$ (i.e. $\delta B_y B_{0y} > 0$), and the firehose limit, in regions where $\delta\boldsymbol{B}\cdot\boldsymbol{B}_0 < 0$ ($\delta B_y B_{0y} < 0$). Note that the factor $\gamma/(c_s k)^{-1} \sim \beta_0^{-1/2}(v_A k/\gamma)^{-1}$ in (3.6) arises due to the smoothing effect of the heat fluxes and reduces Δ significantly (for example, in the CGL model where $q_\perp = q_\parallel = 0$, $\Delta \approx 3\delta B_y/B_0$ is much larger than (3.6)). The linear phase ends as Δ approaches the microinstability limits $|\Delta| \sim \beta^{-1}$ and becomes flattened by growing mirror and firehose fluctuations. Assuming the mode grows at the scale that maximizes the growth rate, $k_{max} v_A/\Omega \sim \beta_0^{-1/6}$ (see (A 2) and figure 7), these limits are reached when $\delta B_y \sim \beta^{-2/3} B_0$, or when $\delta B_x \sim \beta^{-1/3} B_0$ (since $\delta B_x \sim \beta_0^{1/3}\delta B_y$ for these fastest-growing modes; see (A 4)–(A 7)). At this point, the perturbation of B due to δB_x is similar to that due to δB_y, meaning that both components contribute to the pressure anisotropy.[7]

(2) *Pressure anisotropy limited, with $\delta B_y < B_{0y}$.* In the limit that the mirror and firehose fluctuations efficiently constrain the growing $|\Delta|$, the pressure profile will develop a step function profile in space between the mirror limit, $\Delta \approx 1/\beta$, and the firehose limit $\Delta \approx -2/\beta$ (see figure 3b at $t = 12.5\ \Omega^{-1}$). A key effect of these limits is that they suppress the influence of the $\delta p_\perp$ and $\delta p_\parallel$ perturbations on the mode evolution. Without such pressure perturbations, the MRI reverts back to standard, MHD-like behaviour characteristic of the vertical-field MRI (this can be seen, for example, by artificially suppressing $\delta p_{\perp,\parallel}$ perturbations in a calculation of the $B_{0y} \neq 0$ KMRI dispersion relation). Specifically, the growth rate approaches zero for $kv_A \lesssim \Omega$ and peaks at smaller scales $kv_A \sim \Omega$. Thus, the long-wavelength linear modes are significantly stabilized (i.e. γ at low k is small) and the mode moves to shorter wavelengths. Such behaviour is expected intuitively because the azimuthal pressure force, which is the cause of the enhanced low-k linear growth rate (Q02; Balbus 2004), is limited by the mirror and firehose fluctuations. Because the standard MRI grows with the perturbed energies in approximate equipartition, δB_y must 'catch up' to δB_x, and both of these must catch up to the velocity perturbations (which grow linearly with $\delta u_x \sim \delta u_y \sim \beta_0^{1/2}\delta B_y$) during this phase of evolution (in other words, $\delta\boldsymbol{u}$ grows more slowly than $\delta\boldsymbol{B}$). This picture is confirmed by 1-D numerical calculations, with the growth of $\delta\boldsymbol{u}$ decreasing significantly as shorter wavelengths take over; see figure 3(a), Region 2. We also see smaller-scale perturbations growing on top of the longer-wavelength mode in figure 3(b) at $t\Omega = 12.5$ (e.g. around $z = 0.2$ and $z = 0.85$), particularly in those regions at the firehose limit where the MRI preferentially grows at smaller scales because $\Delta p < 0$. Note that the mode cannot be stabilized completely during this phase because the MRI growth rate on a background Δp, though small, is non-zero as $k \to 0$.

3. $\delta B_y > B_{0y}$. As the amplitude of δB grows larger than the background B_{0y} field, the mode enters a second phase of nonlinear evolution. With the field-line direction dominated by the perturbation, the presence of a background B_{0y} loses its dynamical

---

[7]There is a minor ambiguity here because, while the perturbation to B due to δB_y perturbs Δp in both the positive (mirror) and negative (firehose) directions, that due to δB_x perturbs Δp only in the positive direction (it is proportional to δB_x^2). *A priori*, it is thus unclear whether the system will always reach the firehose limit, or whether the decrease in B_y can be offset by the increase in B_x. However, it seems that once the nonlinearity starts becoming important, the rate of change of δB_y increases sufficiently fast (while that of δB_x slows; see figure 3a around $t\Omega \approx 12$) so as to cause the contribution from δB_y to dominate and Δp to reach the firehose. Various tests, similar to that shown in figure 3 but with different β_0 and B_{0y}/B_{0z}, have confirmed that this picture holds so long as β_0 is sufficiently large.

importance and the mode behaves similarly to the vertical-field case, growing at $k v_A \sim \Omega$. In addition, because the magnitude of the magnetic field is now growing everywhere in space, Δ becomes everywhere positive and will be limited only by the mirror instability; see figure 3(b) at $t = 21\ \Omega^{-1}$. As with the vertical-field MRI, when the perturbation amplitude dominates the total B, the pressure anisotropy $\Delta p \approx (\delta B_x^2 + \delta B_y^2)/8\pi$ does not cause significant nonlinear modifications, because $\delta \boldsymbol{B} \cdot \nabla \delta \boldsymbol{B} = 0$ for an MRI channel mode.

4. *Compressibility effects.* There is no 1-D mechanism to halt the growth of the mode until δu approaches the sound speed ($\delta B_x \sim \delta B_y \sim \beta^{1/2} B_0$). Thus, the mode behaves similarly to the vertical-field MRI, with large variations in ρ. The profiles that develop have the same characteristic shape as those seen in figure 2(d) (cf., figure 3b at $t\Omega = 24$).

Each of the four stages discussed above can be seen in the mode energy evolution, shown in figure 3(a). In contrast to the calculation of the vertical-field MRI evolution (figure 2), we begin from random large-scale initial conditions at much higher $\beta_0 = 5000$ (with $B_{0y} = B_{0z}$), so as to clearly distinguish between the different regions of evolution and allow the smaller scale modes to grow after Δ reaches the microinstability limits. While the details of the process described above will be modified depending on a variety of factors – e.g. the mode wavelength in comparison to the domain, the spectrum of the initial conditions, and the value of B_{0y}/B_{0z} – the basic concepts and phases of evolution should be generally applicable. It is also worth noting that, at the large values of β for which our arguments are most applicable, the mode will likely collapse into turbulence before the final nonlinear stage where compressibility is important (see § 4).

3.3.2. *Weakly collisional (Braginskii) regime*

As with the vertical-field MRI in the Braginskii regime (§ 3.2.2), there are two different Braginskii sub-regimes: (i) if $\bar{v}_c \equiv v_c/S \ll \beta^{1/2}$, the instability grows at a similar rate to the collisionless instability (and the heat fluxes play an important dynamical role), or (ii) if $\bar{v}_c \gg \beta^{1/2}$, the growth rate of the MVI is reduced, reaching the collisional (standard MHD) regime when $\bar{v}_c \sim \beta$ (see figures 1–3 of Sharma *et al.* 2003). To understand this latter point – that the Braginskii MRI becomes MHD-like when $\bar{v}_c \gtrsim \beta$ – we compare the Lorentz force, $\boldsymbol{B}_0 \cdot \nabla \delta \boldsymbol{B} = \nabla \cdot (\boldsymbol{B}_0 \delta \boldsymbol{B})$, to the pressure-anisotropy force $\nabla \cdot (\hat{\boldsymbol{b}} \hat{\boldsymbol{b}} \Delta p)$ that arises from the (linear) Δp induced by the KMRI mode,

$$\Delta p \sim \frac{p_0}{v_c} \frac{1}{B} \frac{\mathrm{d}B}{\mathrm{d}t} \sim \frac{p_0}{v_c} \frac{1}{B_0} \frac{\mathrm{d}\delta B}{\mathrm{d}t} \sim \frac{\beta}{v_c} \gamma B_0 \delta B(t), \qquad (3.7)$$

where $B_0^2 = B_{0y}^2 + B_{0z}^2$ and we have assumed $B_{0y} \sim B_{0z}$. Note that we have neglected the heat fluxes in (3.7), which act to reduce Δp (see (3.6)), as is appropriate for the high-collisionality regime (see § B.4). We see from (3.7) that the pressure-anisotropy stress is larger than the Lorentz force (and thus important for the mode's evolution) only if $\bar{v}_c \lesssim \beta$, as expected (Sharma *et al.* 2003).

Numerical experiments (not shown) have revealed that, in the moderate-collisionality regime $\bar{v}_c \equiv v_c/S \ll \beta^{1/2}$, the Braginskii KMRI behaves similarly to a truly collisionless mode (this should be expected based on the arguments above and in § 3.2.2). As described in § 3.2.2, at very large amplitudes, $\delta B > B_0$ (Region 3), the evolution differs from a collisionless mode once $\delta B \gtrsim (\beta_0/\bar{v}_c)^{1/2} B_0$ (the growing mode can no longer

sustain Δp at the mirror limit). In the high-collisionality regime, $\bar{\nu}_c \gtrsim \beta^{1/2}$, the linear mode itself transitions back to the standard MHD MRI, and much of the discussion above loses its relevance. In particular, the most-unstable mode moves to larger scales as $\bar{\nu}_c$ increases (see figure 2*b* of Sharma *et al.* 2003). This implies that the sudden reduction in the scale of the mode when $\Delta p \sim B^2$ (see figure 3*b* between $t \approx 12.5$ and $t \approx 21$) is much less relevant. The mode causes Δp to reach the mirror and firehose limit at some amplitude $\delta B \lesssim B_0$ (with the exact point depending on $\bar{\nu}_c/\beta$) and then transition to the behaviour discussed in § 3.2.2 once $\delta B \gtrsim B_0$.

3.4. *General discussion of 1-D nonlinearities*

With the diverse assortment of nonlinear effects outlined in the previous sections, it seems prudent to conclude with a discussion of some overarching ideas. As is generally the case in high-β collisionless plasma dynamics (e.g. Schekochihin & Cowley 2006; Squire *et al.* 2016), nonlinearity can be important for perturbation amplitudes far below what one might naively expect. For the MRI in the collisionless regime, this occurs a factor of $\sim\beta_0$ (or $\sim\beta_0^{7/6}$ for δB_y with $B_{0y} \neq 0$) below where nonlinear effects become important in standard MHD. However, we have also seen that, in all cases considered, the KMRI (or MVI) always reverts to MHD-like evolution at large amplitudes due to the anisotropy-limiting response of the mirror and firehose instabilities (e.g. Kunz *et al.* 2014*a*). This behaviour has also been seen in fully kinetic 2-D simulations (Riquelme *et al.* 2012). More specifically, this arises because of the form of the pressure anisotropy, *viz.* $\Delta p = B^2/8\pi$, when it is limited at the mirror threshold. If B is dominated by the mode itself ($B^2 \approx \delta B^2$), then the anisotropic stress in the momentum equation (2.2),

$$\nabla \cdot (\Delta p \hat{\boldsymbol{b}}\hat{\boldsymbol{b}}) = \frac{1}{8\pi}\nabla \cdot (B^2 \hat{\boldsymbol{b}}\hat{\boldsymbol{b}}) \approx \frac{1}{8\pi}\delta\boldsymbol{B} \cdot \nabla \delta\boldsymbol{B}, \tag{3.8}$$

acts like an additional Lorentz force, which is zero for the MRI channel mode (Goodman & Xu 1994). This implies that the pressure-anisotropy effects that are critical to the difference between the KMRI and the MRI in linear theory become unimportant once $\delta B \gtrsim B_0$. Due to this, a large-amplitude collisionless KMRI channel mode is an approximate nonlinear solution (of the LF equations), as in MHD, until its amplitude approaches the sound speed (there is a minor complication in the Braginskii regime; see § 3.2.2). Thus, the effect of compressibility on the large-amplitude mode structure – if this occurs before breakdown into turbulence – looks nearly identical in the MHD and kinetic models, with either a Braginskii or LF closure, and with or without azimuthal fields (this structure is shown in figure 2*d*). Very similar structures are also seen at large amplitudes in fully kinetic simulations (Kunz *et al.* 2014*b*).

In contrast, the effect of the nonlinearity at intermediate amplitudes $\delta B \lesssim B_0$ differs between plasma regimes (collisionless and Braginskii) and background field configurations. For modes growing in a purely vertical background field, the nonlinear modification of the mode is modest, so long as the mirror fluctuations limit Δ to be close to $1/\beta$. However, even moderate overshoot past the mirror limit – for example, as might occur in numerical simulations due to insufficient scale separation between Ω_i and Ω, see § 6 – can cause quite strong modifications and/or cause the mode to move to longer wavelengths. Modes evolving in a mixed-vertical–azimuthal background field behave very differently, because the pressure perturbation participates directly in the linear instability (Q02). Upon reaching the mirror and firehose microinstability limits, the pressure perturbation can no longer contribute to the

linear growth and the mode moves towards the smaller scales characteristic of the standard MRI once $\delta B_y \gtrsim \beta^{-2/3} B_0$ (or $\delta B_x \gtrsim \beta^{-1/3} B_0$). This transition is illustrated graphically in figure 3.

4. Saturation into turbulence

In the previous section we have argued that kinetic physics does not offer alternate routes for the saturation of MRI modes in one dimension. In particular, in all cases considered – purely vertical or mixed-vertical–azimuthal field, in both the Braginskii and collisionless limits – the final stages of mode evolution are similar to those seen in standard MHD, with the growing mode becoming close to a nonlinear solution (aside from the effects of compressibility). We must therefore consider alternate means for the saturation of the MRI, in particular 3-D turbulence. This conclusion is supported by the fully kinetic simulations of Riquelme *et al.* (2012) and Kunz *et al.* (2014*b*), in which the 2-D KMRI was seen to grow to very large amplitudes.

In this section, we are concerned with how a growing mode breaks up at large amplitudes into 3-D turbulence. This problem is somewhat separate from the study of the turbulent state itself (which we do not consider here), and has been studied by a variety of authors in terms of 'parasitic modes' (e.g. Goodman & Xu 1994, Latter *et al.* 2009, Pessah & Goodman 2009). These are 3-D secondary instabilities that feed off the large gradients in the growing MRI channel mode, acting to disrupt the mode and seed its transition into turbulence. While the relevance of parasitic modes to transport in the turbulent saturated state has been controversial (e.g. Bodo *et al.* 2008, Latter *et al.* 2009, Pessah & Goodman 2009, Longaretti & Lesur 2010), they are nevertheless a helpful theoretical tool for understanding the initial saturation phase.

The question we address here is whether one should expect any striking differences (compared to MHD) in this initial saturation phase of the KMRI because of differences in the behaviour of parasitic modes brought about by pressure anisotropy. Our conclusion – within the limitations of the LF model (§ 2) – is that there are not significant differences. We also argue that the observations of larger transient channel amplitudes in S06 are explained through the modes' increase in wavelength at large amplitudes due to 1-D pressure-anisotropy nonlinearities (see § 3.2).

Because of this null result, and given the simplifications inherent to our fluid-based model, we keep our discussion brief. We do, however, reach these conclusions through two separate methods: (i) a study of the effect of a mean Δp on linear parasitic-mode growth rates in a sinusoidal channel mode, and (ii) 3-D nonlinear simulations using the modified version of the Zeus code from S06. We thus feel that the general conclusions reached here are relatively robust. That being said, due to the variety of other effects that may be present in a true collisionless kinetic plasma, as well as the strong dependence of MHD MRI turbulence on microphysics (e.g. magnetic Prandtl number; Fromang *et al.* 2007, Meheut *et al.* 2015), we do not necessarily claim that the initial stages of 3-D KMRI saturation should be similar to its MHD counterpart. Rather, our conclusion is more modest: there are no significant differences due to pressure anisotropy and heat fluxes (i.e. those kinetic effects contained within the LF model).

4.1. *Linear parasitic-mode growth rates*

In this section we directly calculate parasitic-mode growth rates for MRI and KMRI channel modes in a vertical background magnetic field. We do not consider a mixed-azimuthal–vertical background field configuration here primarily because the

1-D results of § 3.3 suggested that such modes are always relatively disordered when they reach large amplitudes anyway, due to their strong nonlinear disruption (from long wavelengths to short wavelengths) when $\delta B_y \sim B_y$ (see, e.g. figure 3b). Thus the very idealized linear problem, based on purely sinusoidal background profiles, is presumably much less relevant for this case (we rectify this omission in the 3-D simulations below; see figure 6b).

Motivated by previous MHD studies (Goodman & Xu 1994; Latter *et al.* 2009, 2010; Pessah & Goodman 2009), we consider 3-D linear perturbations, $f(\boldsymbol{x}) = f_{k_x k_y}(z) \exp(ik_x x + ik_y y)$ for $f = \{\boldsymbol{u}', \boldsymbol{B}', \rho', p'_{\perp,\parallel}\}$, evolving on top of a channel-mode background ($\delta \boldsymbol{u}$ and $\delta \boldsymbol{B}$ from (3.1), with δB_0 a free parameter). That is, we decompose the fields as

$$
\left.
\begin{aligned}
\boldsymbol{u} &= -Sx\hat{\boldsymbol{y}} - \sqrt{\frac{3}{5}} \frac{\delta B_0}{\sqrt{4\pi\rho}} \sin(kz)(\hat{\boldsymbol{x}} + \hat{\boldsymbol{y}}) + \boldsymbol{u}', \\
\boldsymbol{B} &= B_0\hat{\boldsymbol{z}} - \delta B_0 \cos(kz)(\hat{\boldsymbol{x}} - \hat{\boldsymbol{y}}) + \boldsymbol{B}', \\
\rho &= \rho_0 + 0 + \rho', \\
p_\perp &= p_0 + \delta p_{\perp 0} + p'_\perp, \\
p_\parallel &= p_0 + \delta p_{\parallel 0} + p'_\parallel,
\end{aligned}
\right\}
\tag{4.1}
$$

with $k = 2\pi/L_z$, and linearize (2.1)–(2.7) in $\boldsymbol{u}'$, $\boldsymbol{B}'$, ρ' and $p'_{\perp,\parallel}$. (For simplicity, we ignore spatial variation in $\delta p_{\perp,\parallel 0}$; see discussion below.) The resulting equations are solved numerically in a box with dimensions[8] $(L_x, L_y, L_z) = (4, 4, 1)$, on a 16×16 grid of Fourier modes in the homogeneous x and y directions, and with a pseudospectral method and 64 modes in the inhomogeneous z direction. Hyperviscous damping is used to remove energy just above the grid scale. We initialize with random noise in all variables, and evolve in time until $t = 10\Omega^{-1}$ (by which time the most-unstable parasitic eigenmode mostly dominates). Fitting an exponential to the energy evolution at later times yields the growth rate γ of the least-stable parasitic mode. Intuitively, a large parasitic-mode growth rate should be associated with rapid collapse of the channel mode into MRI turbulence, because the parasitic modes will quickly 'overtake' the mode itself, with their 3-D structure acting as a seed for the turbulence. Further, as the MRI mode grows (i.e. as δB_0 increases) the parasitic growth rates should increase, since there are stronger gradients of $\delta \boldsymbol{u}$ and $\delta \boldsymbol{B}$ to feed the instabilities.

To assess the impact of the pressure anisotropy, we apply a spatially constant background pressure anisotropy $\Delta p_0 = \delta p_{\perp 0} - \delta p_{\parallel 0}$ in the KMHD models and calculate the resulting change in the maximum parasitic growth rate with Δp_0. A strong variation in growth rate with Δp_0 would indicate that the saturation into turbulence is likely to depend sensitively on the self-generated pressure anisotropy, and thus differ strongly between collisional and collisionless plasmas. Of course, as discussed in § 3, there will be spatial variation in Δp at large δB_0, so the study here should be considered an approximation to the full problem, considering only the simplest effects. Similarly, we neglect the influence of the background shear on the parasitic modes (this is common in previous MHD analyses), because without this simplification the resulting time dependence of k_y implies that an analysis in terms of eigenmodes is incorrect (one should consider transient, or non-modal, growth; Schmid 2007, Squire & Bhattacharjee 2014a,b). This assumption is not truly valid except at very large mode amplitudes when $\delta \boldsymbol{u}$ dominates strongly over the mean shear, although we expect to capture the correct qualitative trends when the parasitic growth

---

[8]The fastest-growing parasitic modes generally have a wavelength several times that of the channel, necessitating a wide box (Bodo *et al.* 2008; Pessah & Goodman 2009).
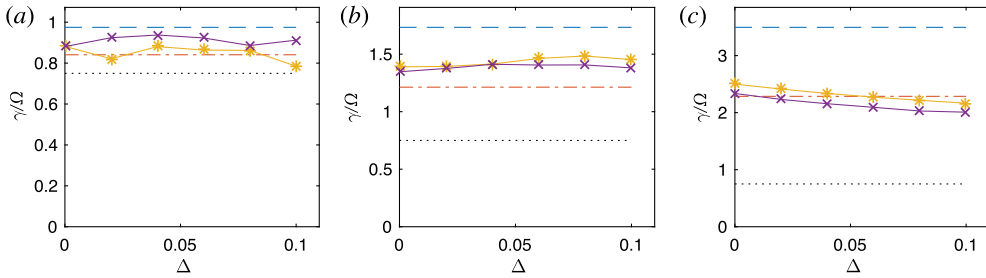
FIGURE 4. Maximum parasitic growth rates γ/Ω as a function of $\Delta = (\delta p_{\perp 0} - \delta p_{\parallel 0})/p_0$ for $\beta_0 \approx 90$ ($B_{0z}/\sqrt{4\pi\rho_0} = 0.15 c_s$) for (a) $\delta B_0/\sqrt{4\pi\rho_0} = 0.5 c_s \approx 3.3 B_{0z}$, (b) $\delta B_0/\sqrt{4\pi\rho_0} = c_s \approx 6.7 B_{0z}$, (c) $\delta B_0/\sqrt{4\pi\rho_0} = 2 c_s \approx 13.3 B_{0z}$. Note that $\Delta = 0.1$ would correspond to a plasma fixed at the mirror limit in a constant background field $B_0 \approx \sqrt{8\pi\Delta p_0} \approx 0.45 c_s \sqrt{4\pi\rho_0}$ (but note that the channel-mode field varies sinusoidally). In each figure the yellow stars illustrate the growth rate in KMHD without heat fluxes (i.e. CGL, $q_\perp = q_\parallel = 0$), while purple crosses illustrate KMHD growth rates including the simple model (2.12) for the heat fluxes. For comparison, the dashed blue line shows the incompressible MHD result and the dash-dotted red line shows the isothermal compressible MHD result (each at $\Delta = 0$). The dotted black line is the MRI channel-mode growth rate $\gamma/\Omega = 3/4$. Evidently, the variation of γ with Δ is modest, and is probably too small to be of much consequence to MRI saturation.
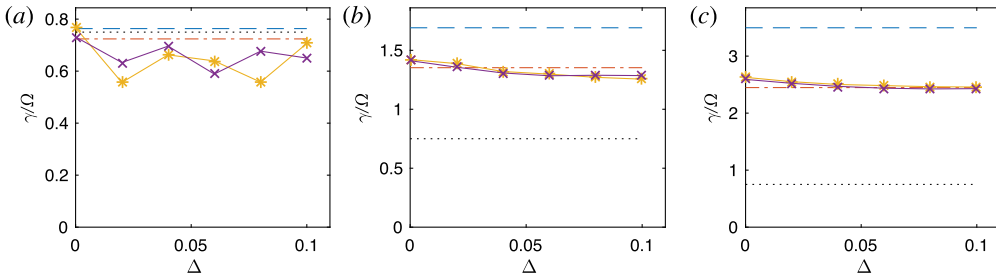

FIGURE 5. As in figure 4 but with a background field $\beta_0 \approx 800$ ($B_{0z}/\sqrt{4\pi\rho_0} = 0.05 c_s$). Although a growing MRI mode would have a shorter wavelength at this B_{0z}, which will make the parasitic modes more unstable at a given amplitude due to the larger gradients, we choose to keep the same $k = 2\pi/L_z$ as figure 4 to provide a direct comparison (recall also from § 3 that the mode wavelength can increase during evolution).

rate is larger than the shearing rate. As mentioned above, given that the pressure anisotropy appears to cause little change to growth rates, we deliberately keep this section brief, postponing to possible future work the detailed study of the mode structure and morphology (e.g. Kelvin–Helmholtz versus tearing-mode instability) or the variation of growth rates with k_x and k_y (Goodman & Xu 1994; Latter *et al.* 2009; Prajapati & Chhajlani 2010).

Figures 4 and 5 illustrate representative examples of γ as a function of $\Delta = (\delta p_{\perp 0} - \delta p_{\parallel 0})/p_0$ and δB_0. In each case the chosen mode energy is of order the thermal energy $\delta B_0/\sqrt{4\pi\rho_0} \sim c_s$ and is larger than the background B_{0z} field. Because of this large δB_0, the parasitic growth rates are mostly larger than the MRI-mode growth rate (dotted line), as required for a parasite to cause the channel mode to break up into turbulence. The maximum of Δ plotted ($\Delta = 0.1$) corresponds to a plasma that is everywhere at

the mirror limit in a constant field of $B_0 \approx \sqrt{8\pi\Delta p_0} \approx 0.45c_s\sqrt{4\pi\rho_0}$, which is larger than the background B_{0z} in each case (but smaller than the maximum δB_0 studied). The first feature that is evident in figures 4 and 5 is the suppression in parasitic-mode growth rates in the kinetic models (solid lines) and compressible fluids (red dash-dotted line), in comparison to incompressible fluids (blue dashed line). This property was also noted for compressible MHD in Latter *et al.* (2009).[9] Aside from this, we see that the differences between the kinetic models (both with and without heat fluxes) and MHD are relatively modest.[10] While there is there is a slight tendency for γ to decrease with Δp at large mode amplitudes, changes in γ of this magnitude are unlikely to make any notable differences in a nonlinear simulation. Furthermore, there does not appear to be any significant change in behaviour at even higher δB_0 (not shown), which leads us to conclude that parasitic modes are broadly unaffected by the kinetic effects contained within the CGL and LF models.

Obviously, the results shown in figures 4 and 5 cover only a small portion of parameter space in a rather idealized setting. In addition to the results shown, we have calculated growth rates across a much wider parameter space in B_{0z}, p_0, δB_0, Δ, k (the channel mode wavelength), small-scale dissipation coefficients (hyper-viscosity, hyper-resistivity and their ratio) and box dimensions. In addition, we have varied the ratio of $\delta \boldsymbol{u}$ and $\delta \boldsymbol{B}$ away from that of the fastest-growing channel mode (i.e. differently from (3.1)), as might be caused, for example, by the effects of the self-generated pressure anisotropy on the mode. Finally, we have also considered parasitic-mode evolution on more angular compressible profiles, similar to those shown in figure 2(d) (Latter *et al.* 2009). In all cases, we have failed to find any significant difference between standard compressible MHD and the CGL or LF models, and so we refrain from presenting these results in any detail here. Of course, these studies have all assumed a spatially constant Δ and ρ_0 profile, which will certainly change results quantitatively in some regimes. It is also possible that there are modes in other regimes (e.g. much longer or shorter wavelength than the KMRI mode), that have not been captured by these studies. Nevertheless, we feel that the general conclusion that the parasitic modes are mostly insensitive to background pressure anisotropy should be robust, given the wide range of parameter space for which this conclusion appears to hold.

4.2. *Nonlinear simulation*

Our second method for probing parasitic-mode behaviour is to simply observe the evolution of a nonlinear KMRI channel mode in three dimensions. The maximum amplitude that such a mode reaches before breaking up into turbulence should give a simple indication of the effectiveness of the parasitic modes. We use the modified version of the ZEUS code described in S06, which solves (2.1)–(2.5) with the LF closure (2.6)–(2.7) and pressure-anisotropy limiters.

---

[9]Although this might be expected to lead to larger saturation amplitudes in compressible MHD in comparison to incompressible MHD, the difference is offset by the more angular channel-mode profiles that develop in compressible MHD. Because these have larger gradients (see figure 2d), this increases the parasitic growth rate and approximately cancels in the decrease in growth rate due to compressibility, leading to similar saturation behaviour. See the appendix of Latter *et al.* (2009) for more details.

[10]The apparent scatter at lower δB_0 is caused by the random initial conditions and relatively small time ($t = 10$) at which we calculate the growth rate. There can be several modes with similar growth rates (particularly ($k_x = 1$, $k_y = 0$) and ($k_x = 2$, $k_y = 0$) in figure 5b), which contribute varying amounts depending on the initial conditions, and thus lead to some scatter in the measured γ. This goes away at higher δB_0 because the much faster growth rates lead to stronger dominance of a single mode by later times.

This method is complementary to that described in the previous section: although it cannot provide detailed information on individual modes or variation with parameters, it is free from some of the caveats of the linear parasitic-mode study (for example, the assumption of spatially homogeneous background density profiles). It also allows us to consider the mixed-azimuthal–vertical field KMRI in a moderately realistic settling (as mentioned above, the stronger effects of 1-D nonlinearities in this case suggest that an idealized parasitic-mode study is not very worthwhile for the azimuthal-field KMRI). Most importantly, 3-D simulations directly address the issue we most care about: is the nonlinear saturation significantly different between the kinetic and MHD models? In S06 the authors noted that there was a significant difference, with MRI modes in kinetic models growing to significantly larger amplitudes before being disrupted, even though the turbulence itself maintained a similar level of angular-momentum transport. While this may appear to be at odds with our findings from the previous section, here we argue that this difference is primarily a consequence of the 1-D effects described in § 3. Specifically, the positive pressure anisotropy can increase the wavelength of the mode well before it reaches saturation amplitudes. This effect was caused by the choice of $\Delta \approx 7/\beta$ for the mirror instability limit in S06, which allows the anisotropies to have a strong dynamical effect before the mirror limit is enforced. For a given mode amplitude, these longer-wavelength modes are attacked more slowly by the parasites, due to the smaller gradients of $\delta\boldsymbol{u}$ and $\delta\boldsymbol{B}$ (Goodman & Xu 1994), thus leading to a larger transient amplitude before the transition into turbulence.

Our studies have deliberately used a set-up that is similar to S06. We initialize with random noise in all variables and a background magnetic field with $\beta_0 = 400$ in a box of dimension $(L_x, L_y, L_z) = (1, 2\pi, 1)$. We take $k_L \approx 14$, which corresponds to capturing Landau damping correctly ($k_\parallel \approx k_L$) for low-amplitude modes with a wavelength of approximately half of the size of the box, and limit the positive pressure anisotropy at $p_\perp/p_\parallel - 1 < \xi_{\mathrm{Mir}}/\beta_\perp$ (this is $\Delta < \xi_{\mathrm{Mir}}/\beta$ for $\Delta p \ll p_0$). With either a purely vertical background field, or a mixed-azimuthal–vertical background field ($B_{0y} = B_{0z}$), we compare the mode saturation between MHD, the LF model with $\xi_{\mathrm{Mir}} = 7$, and the LF model with $\xi_{\mathrm{Mir}} = 1$. The vertical-field LF model runs are identical to runs Zl4 and Zl5 of S06.

Our findings are illustrated in figure 6, which plots the modes' energy evolution in both LF cases and standard MHD, with a purely vertical field (left-hand panel a) and with a mixed-azimuthal–vertical field (right-hand panel b). The key result of this figure is the larger (∼factor 10) overshoot of the vertical-field KMRI mode (panel a) with $\xi_{\mathrm{Mir}} = 7$ (compared to MHD), which disappears at $\xi_{\mathrm{Mir}} = 1$ (i.e. there is effectively no difference between MHD and the LF model with the $\xi_{\mathrm{Mir}} = 1$ mirror limiter). As mentioned above, this leads us to attribute the differences between MHD and the LF model saturation to the difference in the large-amplitude wavelength of the MRI modes. Specifically, the strength of the vertical magnetic field for $\beta_0 = 400$ is such that modes with $k_z = 4\pi/L_z$ dominate during the linear phase, but, with the artificially high mirror boundary $\xi_{\mathrm{Mir}} = 7$, Δ becomes large enough to cause the KMRI mode to increase in scale to the largest in the box by later times (see insets). This does not occur with the standard mirror limit $\xi_{\mathrm{Mir}} = 1$. While not unexpected, these results do show that there are not inherent differences in the parasitic modes' properties between the kinetic (LF) model and MHD for the vertical-field MRI. Examination of mode evolution at a variety of other values for β_0 and ξ_{Mir} (not shown) has produced results that are generally consistent with this idea.

In figure 6(*b*), showing a mixed-azimuthal–vertical background field configuration, we see that the saturation amplitudes of all three cases (the MHD model, and the
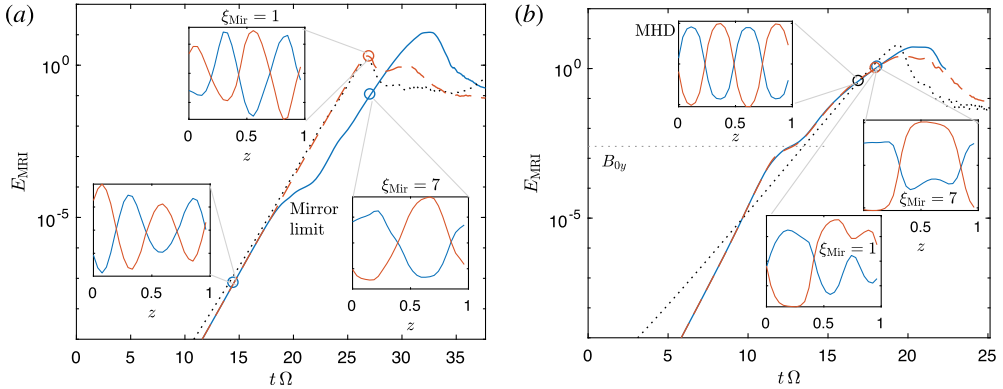
FIGURE 6. Energy of the MRI perturbation, $E_{MRI} = \int dz \, (\rho \, \delta u^2 / 2 + \delta B^2 / 8\pi)$, as a function of time for a set of 3-D ZEUS simulations at $\beta_0 = 400$. We compare the evolution of the LF model (2.1)–(2.7) with mirror limiter $\Delta = 7/\beta$ as used in S06 (blue solid lines), the LF model with mirror limiter $\Delta = 1/\beta$ (red dashed lines) and standard MHD (black dotted lines). The insets show the vertical mode structure (δB_x, blue; δB_y, red) at the times indicated by the circles. Panel (*a*) shows the case with a purely vertical background magnetic field ($B_{0y} = 0$). This illustrates how an artificially high mirror limit ($\Delta = 7/\beta$; blue solid line) causes the mode to move to longer wavelengths after it reaches the mirror limit at $t \approx 17$, which subsequently causes the mode to reach a very large amplitude before saturation. Panel (*b*) shows simulations with an azimuthal background magnetic field ($B_{0y} = B_{0z}$; the dotted line shows the energy of B_{0y}); in this case, all three modes saturate into turbulence at similar amplitudes. Given the relatively disordered mode structure in the kinetic runs (the insets compare the late-time structures of all three cases, as labelled), this behaviour is consistent with the idea that there are not major differences between the parasitic modes' properties in the kinetic (LF) model and MHD (see text for further discussion). Note that the time scale of the MHD case in panel (*b*) has been shifted to the left, so that all three modes reach saturation amplitudes at a similar time (the linear growth of the KMRI mode is faster, see figure 1).

$\xi_{Mir} = 1$ and $\xi_{Mir} = 7$ LF models) are similar. This seems to be because even at large amplitudes, the KMRI modes are relatively disordered and each have both $k = 2\pi/L_z$ and $k = 4\pi/L_z$ components, while the MHD mode is nearly a pure $k = 4\pi/L_z$ mode. This more disordered KMRI state is expected based on the 1-D analysis of § 3.3: the mode is strongly disrupted as δB_y surpasses B_{0y}, and has not had time to 'pick out' the fastest-growing mode (see also figure 3*b*). Thus although the MHD mode might be more easily attacked by the parasitic modes (given its smaller scale), the more disordered KMRI modes are further from being nonlinear solutions, and thus more easily evolve into turbulence. The net result is that they all saturate at approximately the same amplitude. As further evidence for this scenario, we see that the $k = 2\pi/L_z$ component of the $\xi_{Mir} = 7$ mode is larger than that of the $\xi_{Mir} = 1$ mode (as expected because Δp is larger, increasing the effective magnetic tension), explaining its slightly higher saturation amplitude. Thus, these mixed-azimuthal–vertical field KMRI results also suggest that there is little difference between the parasitic-mode properties in the kinetic (LF) model and MHD. Again, we have examined mode evolution at various other values for β_0 and ξ_{Mir} (not shown) and seen similar results; however, to truly study this case in detail would require much higher resolution simulations (so as to allow higher β_0; see figure 3), which are beyond the scope of this work.

Overall, we see that all of our calculations – both of linear parasitic-mode growth rates in idealized settings and 3-D studies using the full nonlinear LF model – are consistent with the idea that parasitic modes are not strongly affected by the kinetic effects contained within the fluid models considered in this work. This seems to be the case for both the vertical-field KMRI and the mixed-azimuthal–vertical field KMRI (although we did not study the parasitic modes directly for the mixed-field case). An obvious caveat of this conclusion is that we have considered only the LF model in this work, and future studies with fully kinetic methods (in particular, those that can correctly capture plasma microinstability saturation) are needed to shed light on whether our conclusions also hold for truly collisionless plasmas.

5. Kinetic effects not included in our models

Our approach throughout this paper has been to consider only the simplest kinetic effects, in particular those arising from a self-generated gyrotropic Δp. Further, the Landau-fluid models used for much of the kinetic modelling do not correctly capture the all-important firehose and mirror microinstabilities, and we have resorted to applying phenomenological hard-wall limits as commonly used in previous works (S06; Sharma *et al.* 2007, Santos-Lima *et al.* 2014). In this section we briefly outline some physical effects that are not included in our model, most of which must be examined, in one way or another, through fully kinetic simulations (e.g. Kunz *et al.* 2016).

Mirror and firehose evolution. Recent kinetic simulations and analytical calculations (Kunz *et al.* 2014a; Hellinger *et al.* 2015; Rincon *et al.* 2015; Melville *et al.* 2016) paint an interesting picture of how the firehose and mirror instabilities saturate, with each going through a regime where fluctuations grow secularly with little particle scattering, followed by a saturated regime in which the microinstabilities strongly scatter particles due to sharp small-scale irregularities in the magnetic field. The mirror instability is particularly interesting, both because it is more important than the firehose for MRI dynamics (since $\mathrm{d}B/\mathrm{d}t > 0$ quite generally), and because it grows secularly over macroscopic time scales (i.e. for $t \sim |\nabla \boldsymbol{u}|^{-1}$) before saturating and scattering particles (Kunz *et al.* 2014a; Rincon *et al.* 2015; Riquelme *et al.* 2015; Melville *et al.* 2016). This may add another time scale and nonlinear feature into the 1-D MRI evolution described in § 3, whereby the effective collisionality is strongly enhanced some time $t \sim \Omega^{-1}$ after Δp initially reaches the mirror limit. It is unclear if there will be a significant change in macroscopic behaviour with the onset of particle scattering, and fully kinetic MRI simulations with large scale separations $\Omega / \Omega_i \gg 1$ are needed to address this issue (see § 6 for further discussion).

Other kinetic instabilities. There are a variety of other pressure-anisotropy-induced kinetic instabilities that we have ignored throughout this work. For the ion dynamics, the most important of these is likely the ion-cyclotron instability (see, e.g. Gary, McKean & Winske 1993). While general theoretical analysis (Gary *et al.* 1997; S06) and solar-wind observations/theory (Kasper, Lazarus & Gary 2002; Bale *et al.* 2009; Verscharen *et al.* 2016) suggest that the ion-cyclotron instability is less important than the mirror instability when $T_e \sim T_i$ and $\beta_0 \gtrsim 1$, it may become more important at lower T_e/T_i (as expected in low-luminosity accretion flows). In particular, the works of Sironi (2015) and Sironi & Narayan (2015) suggest that there is a transition around $T_e/T_i \lesssim 0.2$ (or somewhat lower when $\beta_i \gtrsim 30$) below which the ion-cyclotron instability dominates over the mirror instability in regulating pressure anisotropy (this

behaviour is at least partially accounted for by the linear effects of electron pressure anisotropy; see Pokhotelov *et al.* 2000, Remya *et al.* 2013). At least for lower β_i plasmas, this will modify the threshold at which the pressure anisotropy is nonlinearly regulated (see §2.3 of S06) and change the microphysical mechanism through which this regulation occurs (Sironi & Narayan 2015).

Non-thermal distributions. Having focused on fluid models, we cannot address the many interesting questions surrounding non-thermal particle distributions that might develop. Strong non-thermal distributions have been seen in a variety of kinetic simulations (Riquelme *et al.* 2012; Hoshino 2015; Kunz *et al.* 2016), perhaps due to magnetic reconnection.

Electrons. We have completely neglected any discussion of electron dynamics throughout this work. This can be loosely justified either when the electrons are (significantly) colder than ions, or in a weakly collisional regime, when ions dominate the anisotropic stress in the momentum equation due to the higher electron collisionality. However, even in such regimes, where the anisotropic stress due to elections is nominally subdominant to that of the ions, there may be additional subtleties induced by their thermodynamics. For example, the ion-cyclotron instability increases in importance compared to the mirror instability when $T_e \ll T_i$ (see above, Sironi & Narayan 2015). Further, the induced electron-pressure-anisotropy stress will presumably not be efficiently regulated by ion-scale instabilities, potentially allowing the anisotropic electron stress to grow to dynamically important values even if $T_e \ll T_i$, and/or exciting electron instabilities (e.g. the electron whistler instability; Kim *et al.* 2017; Riquelme, Osorio & Quataert 2017). In addition to the possible influence of electron-anisotropy instabilities and stresses, there are a variety of important questions to explore related to the proportion of viscous heating imparted to ions and electrons in RIAFs (e.g. see Sharma *et al.* 2007, Ressler *et al.* 2015, Sironi 2015, Riquelme *et al.* 2017).

Non-gyrotropic effects. As the temporal and spatial scales of the MRI approach the gyro-scale, the approximation of gyrotropy – that the pressure tensor is symmetric about the magnetic-field lines – breaks down. In this case, either more complex fluid models (Passot, Sulem & Hunana 2012) or fully kinetic treatments are needed to understand any key differences due to non-gyrotropic effects. While such effects are unlikely to be astrophysically important in current-epoch disks (where the separation between macroscopic scales and the gyro-scale is often $\sim 10^{10}$ or more), they may be important for understanding the amplification of very weak ($\beta \gtrsim \Omega_i/\Omega$) fields in the high-redshift universe (Heinemann & Quataert 2014; Quataert *et al.* 2015). In addition, numerical simulations will always have limited scale separations (in order to resolve both the macroscopic scales and the gyroradius), and knowledge of such effects could be important for the complex task of characterizing the limitations of kinetic simulations (see §6.4).

6. Implications for the design of kinetic MRI turbulence simulations

In light of the above caveats concerning detailed kinetic effects absent in our models, it is clear that continued efforts to more rigorously simulate KMRI turbulence are needed. In this section, we leverage the results of this paper, as well as those from existing kinetic simulations of the KMRI and of Larmor-scale velocity-space instabilities, to provide some guidance for such efforts. Driving the discussion is a recognition that achieving a healthy scale separation in a kinetic simulation of

magnetorotational turbulence is numerically expensive, perhaps prohibitively so. We thus focus primarily on non-asymptotic behaviour that might occur when Ω/Ω_i is not sufficiently small, and provide some estimates for what Ω/Ω_i must be smaller than in order to capture the effects predicted in this paper. We stress that the asymptotic regime focused on in this paper is likely the most astrophysically relevant one, even if it is difficult to realize in fully kinetic simulations.

6.1. *Pressure-anisotropy overshoot due to finite scale separation*

First, in order for the mirror instability to effectively regulate the positive pressure anisotropy during the growth of KMRI, the growth of the mirrors must deplete the anisotropy faster than it is being adiabatically replenished by the KMRI. This requires $\gamma_m/\gamma_{\mathrm{kmri}} > 1$, where γ_m and γ_{kmri} are the growth rates of the mirror instability and KMRI, respectively. The maximum growth rate of the mirror instability is given by $\gamma_m \sim \Omega_i \Lambda_m^2$, where $\Lambda_m \doteq \Delta - 1/\beta_\perp$ is positive when the plasma is mirror unstable (Hellinger 2007). Thus, we require $\Lambda_m > (\gamma_{\mathrm{kmri}}/\Omega_i)^{1/2}$ for the mirror instability to outpace the KMRI-driven production of positive pressure anisotropy. For the vertical-field case, $\gamma_{\mathrm{kmri}} = S/2$ at maximum growth, and so we require $\Lambda_m > (S/2\Omega_i)^{1/2}$.[11] When there is an azimuthal magnetic field present, $\gamma_{\mathrm{kmri}} \approx (2S\Omega)^{1/2}$ at maximum growth, and so we require $\Lambda_m > (S/\Omega_i)^{1/2} (2\Omega/S)^{1/4} \approx (S/\Omega_i)^{1/2}$. Of course, in this case we must also contend with the firehose instability in regions where $\Delta \propto \delta B_y < 0$ (see (3.6)), for which the instability criterion is $\Lambda_f \doteq \Delta + 2/\beta_\parallel < 0$. With $\gamma_f \sim \Omega_i |\Lambda_f|^{1/2}$ as the growth rate for the fastest-growing oblique firehose (Yoon *et al.* 1993; Hellinger & Matsumoto 2000), we require $|\Lambda_f| > (S/\Omega_i)^2 (2\Omega/S) \simeq (S/\Omega_i)^2$ for the firehose instability to outpace the KMRI-driven production of negative pressure anisotropy. The parallel-propagating firehose has $\gamma_f = \Omega_i |\Lambda_f|$ as its maximum growth rate (e.g. Davidson & Völk 1968; Rosin *et al.* 2011), and thus grows slower than its oblique counterpart for $|\Lambda_f| \lesssim 1$.

We now determine whether these criteria place prohibitive constraints on kinetic simulations. For the vertical-field KMRI, $\Delta \sim (\delta B/B_0)^2$ (see (3.2)), and so the mirror instability will grow fast enough to deplete the pressure anisotropy $\Lambda_m \to 0^+$ when

$$\left(\frac{\delta B}{B_0}\right)^2 \gtrsim \frac{1}{\beta_0} + \left(\frac{S}{\Omega_i}\right)^{1/2}, \qquad (6.1)$$

beyond which the plasma is kept marginally mirror stable (and the results of this paper then follow). The asymptotic limit $(S/\Omega_i)\beta_0^2 \to 0$ was taken throughout this paper to obtain $(\delta B/B_0)^2 \sim 1/\beta_0$ at the mirror instability threshold. The additional factor of $(S/\Omega_i)^{1/2}$ due to overshoot beyond this threshold may be quite appreciable in a contemporary kinetic simulation of the MRI, perhaps ~ 0.1 (e.g. Kunz *et al.* 2016) or even more (e.g. Riquelme *et al.* 2012; Hoshino 2015), and thus might be comparable to, if not larger than, $1/\beta_0$. The situation will, of course, improve as the amplification of the magnetic-field strength by the KMRI increases Ω_i and decreases β. Thus, in the final, turbulent saturated state, the effect of finite scale separation will presumably

---

[11]See the inset of figure 6 in Kunz *et al.* (2014*a*) for a numerical demonstration of the scaling $\max(\Lambda_m) \propto (S/\Omega_i)^{1/2}$, where S is the shear rate at which pressure anisotropy is driven. See also Kunz *et al.* (2016, figure 1*c*) for a demonstration that $\Lambda_m \simeq \Delta \simeq 0.12 \approx (S/2\Omega_i)^{1/2}$ when the mirror modes begin to first deplete the pressure anisotropy driven by the vertical-field KMRI. (Note that our definition for Δ is actually twice as large as the quantity $(p_\perp - p_\parallel)/p_0$ plotted in Kunz *et al.* (2016, figure 1(*c*)), which temporarily peaks at $\simeq 0.07$ before the mirrors are able to drive the pressure anisotropy towards marginal mirror stability. The factor of 2 difference is because of the additional thermal pressure in p_0 from the electrons.)

be less severe than during the early, weakly nonlinear phases that have been the focus of this work; nonetheless, one should at least be aware of the impact of insufficient scale separation on the early phase of the KMRI.

In a mixed-azimuthal–vertical guide field, the KMRI-driven pressure anisotropy is linear in the mode amplitude (see (3.6)). Because, in this case, it is the pressure anisotropy which provides the azimuthal torque to transport angular momentum and drive the instability (rather than the magnetic tension), it matters all the more how efficiently the pressure anisotropy is regulated. If the lack of scale separation allows the pressure anisotropy to grow much beyond the mirror threshold, the instability's behaviour once $\delta B_y \gtrsim \beta_0^{-2/3} B_{0y}$ may be completely different. Let us be quantitative, assuming $B_{0y} \approx B_{0z}$ and that β_0 is sufficiently high ($\beta_{0z} \gtrsim 10^3$ at least) that the scalings derived in appendix A hold. Then, the maximum growth rate of the azimuthal KMRI, $\gamma \approx (2S\Omega)^{1/2}$, occurs at wavenumbers satisfying $|k|v_{Az}/\Omega \approx 2\beta_0^{-1/6}$ (see (A 2)), and the driven pressure anisotropy (3.6) is

$$\Delta \approx \sqrt{\frac{\pi S}{\Omega}} \beta_0^{-1/3} \frac{\delta B_y(t)}{B_0} \left(\frac{2\beta_0^{-1/6}\Omega}{v_{Az}|k|} \right), \tag{6.2}$$

where the final term in parentheses is order unity. Thus, the mirror instability will grow fast enough to deplete the excess positive pressure anisotropy when

$$\left(\frac{\delta B_y}{B_0} \right)^2 \gtrsim \frac{\Omega}{\pi S} \left(\frac{1}{\beta_0^{2/3}} + \frac{S^{1/2}\beta_0^{1/3}}{\Omega_i^{1/2}} \right)^2, \tag{6.3}$$

which may be readily compared to (6.1). The asymptotic limit $(S/\Omega_i)\beta_0^2 \to 0$ was taken throughout this paper to obtain $\delta B_y/B_0 \sim \beta_0^{-2/3}$ at the mirror instability threshold. The additional factor of $(S/\Omega_i)^{1/2}\beta_0^{1/3}$ is due to the necessary overshoot beyond this threshold, which, again, may not be all that small in a contemporary kinetic simulation. For the firehose, the negative pressure anisotropy will be efficiently depleted when

$$\left(\frac{\delta B_y}{B_0} \right)^2 \gtrsim \frac{4\Omega}{\pi S} \left(\frac{1}{\beta_0^{2/3}} + \frac{S^2\beta_0^{1/3}}{2\Omega_i^2} \right)^2, \tag{6.4}$$

which will occur after the mirror criterion (6.3) is satisfied because of its more forgiving threshold (as long as $(S/\Omega_i)^{1/2}$ is small compared to $1/\beta_0$).

6.2. *The impact of pressure-anisotropy overshoot on the KMRI*

One notable impact of these pressure-anisotropy overshoots is on the fastest-growing KMRI-mode wavelength. For the vertical-field case, this wavelength will increase due to the nonlinear pressure anisotropy by an amount $\approx (3/2 + \beta \Lambda_m/2)^{1/2}$. With $\Lambda_m \gtrsim (S/\Omega_i)^{1/2}$ required for the mirrors to outpace the production of anisotropy, this could easily be a factor of several increase unless adequate scale separation is used. For example, having $\beta = 400$ and $S/\Omega_i = 0.01$ would result in a pressure-anisotropy-driven increase in the KMRI wavelength by a factor of ≈ 5. In a computational box with vertical extent $L_z \equiv c_s/\Omega$, this means that a maximally growing mode with $kv_A \simeq \Omega$ and $\gamma \simeq S/2$ would shift from having $\lambda/L_z \approx 2\pi(2/\beta)^{1/2} \approx 0.4$ to $\lambda/L_z \approx 2$, bigger than the box. The mode's wavelength would, of course, stop increasing once $\lambda/L_z = 1$. But

if, at that point, $\Lambda_m \gtrsim (S/\Omega)/2\pi^2 - 3/\beta$, then all the KMRI modes in the box would be stabilized by the effectively increased magnetic tension. Since Λ_m must grow to $\sim(S/\Omega_i)^{1/2}$ before the mirrors can efficiently relax the pressure anisotropy and thereby remove some of this excess tension, we find that values of $S/\Omega_i \gtrsim [(S/\Omega)/2\pi^2 - 3/\beta]^2$ will ultimately stabilize the KMRI.[12] It is, however, likely that this stabilization would be transient: even if the KMRI stops growing, the mirrors will continue relaxing Δp (albeit rather slowly), and at some point Δp would be sufficiently low so as to render the KMRI unstable again. Finally, we note that if the box does continue to support unstable KMRI modes on the largest scales $\lambda/L_z = 1$, one must ensure that the horizontal extent of the box is large enough to fit the parasitic modes (§ 4.1).

In the azimuthal–vertical-field case, the fastest-growing mode occurs on scales satisfying $k v_{Az}/\Omega \sim \beta_0^{-1/6}$, or $\lambda/L_z \sim \beta_0^{-1/3}$. These scales are larger than those of the standard MRI and the vertical-field KMRI. We have predicted that, as the mirror and firehose instabilities kick in and regulate the pressure anisotropy, the influence of the $\delta p_\perp$ and $\delta p_\parallel$ perturbations on the mode evolution is suppressed and the KMRI reverts back to its standard, MHD-like behaviour. This involves a suppression of long-wavelength MRI modes (i.e. γ_{kmri} decreases for $k v_A \lesssim 1$) and a transition phase in the nonlinear evolution ('Region 2' in figure 3a), in which the mode becomes more MHD-like at smaller scales with the kinetic and magnetic energies in approximate equipartition. If the mirror regularization is especially sluggish due to inadequate scale separation, this phase might be skipped altogether and a $\lambda/L_z = 1$ mode will take the place of what is instead seen in figure 3(b). It is also worth noting that the large value of $\beta_0 = 5000$ used in § 3.3 to accentuate the different regions of evolution would require an especially small value of S/Ω_i in a kinetic simulation.

6.3. *The microphysics of the firehose and mirror instabilities*

A further constraint on the choice of S/Ω_i concerns the means by which mirror/firehose instabilities regulate the pressure anisotropy. In order for these instabilities to efficiently keep the anisotropy near the instability thresholds via the anomalous pitch-angle scattering of particles, the scattering rate must be $\sim S\beta$, and this number must be smaller than Ω_i.

In the case of the firehose instability, when $S/\Omega_i \ll 1/\beta$ the firehose fluctuations saturate at a mean level $\langle|\delta \boldsymbol{B}/B|^2\rangle \sim (\beta S/\Omega_i)^{1/2}$ in a time $\sim[\beta/(S\Omega_i)]^{1/2} \ll S^{-1} \sim \gamma_{\text{kmri}}^{-1}$ (Kunz *et al.* 2014a; Melville *et al.* 2016). This is achieved via pitch-angle scattering of the particles off Larmor-scale firehose fluctuations, which precludes the adiabatic production of pressure anisotropy. In this limit, since local shear in a macroscopic plasma flow will change in time at the rate comparable to the shear itself, one can safely consider the anomalous collisionality associated with the firehose fluctuations to turn on instantaneously, in line with the macroscopic modelling assumption used in this paper. At sufficiently high β and/or S such that $\beta \gtrsim \Omega_i/S$, however, this is no longer true and the firehose fluctuations saturate at an order-unity level independent of either β or S, after growing secularly without scattering particles for one shear time (Melville *et al.* 2016). Thus, for kinetic simulations of MRI turbulence to reliably demonstrate the anomalous-scattering model of pressure-anisotropy regulation used in this work and others (e.g. Sharma *et al.* 2006; Mogavero & Schekochihin 2014; Santos-Lima *et al.* 2014; Chandra *et al.* 2015; Foucart *et al.* 2015), parameters must

---

[12]That is, unless β decreases (or Ω_i increases) by an appreciable amount due to the KMRI-driven field amplification by the time that λ reaches the box size. In this case, we would have $\delta B/B_0 \gg 1$ and other nonlinear effects could become important also (e.g. compressibility).

be chosen such that $S/\Omega_i < 1/\beta$, preferably by a decade or more. Again, satisfying this inequality becomes easier as the KMRI grows the magnetic-field strength. But, for the early phases of evolution, this cautions against setting β_0 too high, because this will impose stiff constraints on an acceptable value of S/Ω_{i0}.

In the arguably more relevant case of the mirror instability, when $S/\Omega_i \ll 1/\beta$ the mirror fluctuations saturate at a mean level $\langle (\delta B/B)^2 \rangle \sim 1$ in a time $\sim S^{-1} \sim \gamma_{kmri}^{-1}$ (Kunz *et al.* 2014*a*; Riquelme *et al.* 2015; Melville *et al.* 2016). While marginal stability and mirror saturation is ultimately achieved via pitch-angle scattering of the particles off Larmor-scale bends at the ends of the magnetic mirrors, there is a long ($\sim S^{-1}$) phase in which the pressure anisotropy is held marginal without appreciable particle scattering. This is achieved by corralling an ever increasing number of particles into the deepening magnetic wells, in which these particles become trapped, approximately conserve their μ as they bounce to and fro, and perceive no average change in B (and thus no generation of net pressure anisotropy) along their bounce orbits. The increase in the large-scale B is offset by the decrease in the intra-mirror B. During this phase of evolution, the mirror fluctuations grow at the rate required to offset the production of pressure anisotropy by the KMRI-driven growth in the large-scale magnetic-field strength. A few things must be satisfied for kinetic simulations of KMRI growth to produce results similar to those predicted in this paper. First, the hard-wall limiter on the pressure anisotropy that we (and others) use must be an adequate (if not complete) representation of the otherwise more complicated mirror-driven regulation. This is particularly true during the μ-conserving phase of the mirror instability: does it matter to the large (i.e. KMRI) scales that an ever-increasing population of trapped particles are ignorant of the KMRI-driven magnetic-field growth during this phase? If not, then fine; simply limit the pressure anisotropy at the mirror instability using an enhanced collisionality, nothing more sophisticated being necessary. But, if so, then an effort must be made in the kinetic simulation to ensure that its results, if different from those predicted in this paper, are truly asymptotic. Namely, since the μ-conserving phase of the mirror instability lasts just one shear time, whereas the KMRI growth phase typically lasts several shear times, there must be enough scale separation so that the mirrors can saturate before $\delta B/B_0$ of the KMRI enters into the nonlinear phases we predicted in §3. Secondly, do the Larmor-scale mirror distortions in the magnetic-field direction greatly affect the efficacy of the heat flow? An answer in the affirmative is suggested by Komarov *et al.* (2016), Riquelme *et al.* (2016), Riquelme *et al.* (2017). But, if the effect of these distortions is simply a reduction in the magnitude of the heat flow, then the footnote in §2.1 applies: our results are not strongly affected. The reason is that, by the time the mirror instability is triggered, the heat flows have already spatially smoothed the pressure anisotropy on the scale of the KMRI mode, fulfilling their main role in influencing the mode evolution.

6.4. *Finite-Larmor-radius effects*

There is additional physics that enters when S/Ω_i is not sufficiently small, which might complicate the evolution of the KMRI beyond that envisaged herein. First, gyroviscous effects become important when $\beta \gtrsim 4\Omega_i/\Omega$ (Ferraro 2007; Heinemann & Quataert 2014). For such β, the polarity of the mean magnetic field influences the stability and MRI growth rates. Without a good scale separation between Ω and Ω_i, finite-Larmor-radius effects might therefore artificially modify the KMRI, even at modest β. Secondly, note that an equilibrium particle distribution function in a strongly magnetized differentially rotating disc can be quite different than

an equilibrium distribution function in an unmagnetized disc. In the latter, a tidal anisotropy of the in-plane thermal motions of the particles is enforced by epicyclic motion in the rotational supported plasma (see § 3.1 of Heinemann & Quataert 2014); this effect goes away in a strongly magnetized plasma, where gyrotropy of the distribution function about the magnetic field is enforced. This is important because, if the initial magnetic field is inclined with respect to the rotation axis (i.e. $b_y \neq 0$, $b_z \neq 1$) and S/Ω_i is not sufficiently small, this tidal anisotropy can function as a field-biased pressure anisotropy and potentially drive mirror fluctuations in the equilibrium state. To wit, the equilibrium field-biased pressure anisotropy is $\Delta \approx (3/2)(S/\Omega_i)(b_y^2 - 1/3)/b_z$ to leading order in S/Ω_i when $b_z \neq 0$. A disc with $b_y = b_z = 1/\sqrt{2}$ would be mirror unstable from the tidal anisotropy alone if $S/\Omega_i \gtrsim 2\sqrt{2}\beta^{-1}$. (A plasma with, say, $\beta_0 = 400$ and $S/\Omega_i = 0.01$ would thus be mirror unstable, even without the KMRI-driven pressure anisotropy.) If the background field is exactly azimuthal, then the field-biased pressure anisotropy $\Delta = S/(2\Omega) > 0$, and any large-β plasma would be trivially mirror unstable, no matter how strongly the plasma is magnetized.

6.5. *The saturated state*

Finally, one must be cognizant of the physical constraints and computational demands not only during the early stages of the KMRI, but also in the saturated state. In going, say, from $\beta_0 \approx 10^3$ to $\beta \approx 4$, as often seen in a typical magnetorotationally turbulent saturated state (e.g. Pessah, Chan & Psaltis 2006), the ion Larmor radius might shrink by a factor between ≈ 4 (if μ is somehow conserved during this process) and ≈ 16 (if μ is not). Increased scale separation is, of course, a good thing, but only to a point. If ρ_i decreases so much that it falls under the numerical grid, then the anomalous particle scattering from ion-Larmor-scale magnetic structures that plays a regulatory role for the pressure anisotropy will be attenuated, fundamentally changing the physics of the mirror and firehose instabilities.

7. Conclusions

A persistent feature of high-β collisionless plasmas is the appearance of nonlinearity due to pressure anisotropy in regimes where similar dynamics in a collisional (MHD) plasma is linear (e.g. Schekochihin & Cowley 2006, Mogavero & Schekochihin 2014, Squire *et al.* 2016). Such behaviour generically arises because, for similar values of the magnetic field, the mechanisms that generate a pressure anisotropy are proportional to the total pressure (e.g. $\mathrm{d}\Delta p/\mathrm{d}t \sim p_0 \, \mathrm{d} \ln B/\mathrm{d}t$ in the collisionless case), while the momentum stresses induced by this anisotropy (i.e. its dynamical effects) depend on Δp itself (i.e. not on $\Delta p/p_0$). Thus a larger background pressure leads to larger anisotropic stresses, which dominate the Lorentz force by a factor $\sim \beta$. This implies that nonlinear effects can become important for very small changes in magnetic-field strength. However, as is well known, once the anisotropy grows beyond $\Delta p \sim \pm B^2$, the firehose and mirror instabilities grow rapidly at ion gyro-scales and limit any further growth in Δp. We are then left with the question of whether the resulting dynamics on large scales is effectively MHD-like (as occurs if the microinstability-limited Δp is dynamically unimportant), or whether there are strong differences compared to MHD. In either case, we can expect that linear instabilities will be nonlinearly modified for amplitudes well below where such modifications occur in MHD.

This work has considered the influence of this physics on the collisionless (kinetic) and weakly collisional (Braginskii) magnetorotational instability (KMRI), focusing on the characteristics of the instability at high β before its saturation into turbulence. Our general motivations have been to:

(i) Understand if there are any alternate (pressure anisotropy related) means for the linear KMRI to saturate in various regimes. Such a mechanism could significantly alter expected angular-momentum transport properties of kinetic MRI turbulence.

(ii) Inform current and future kinetic numerical simulations of the KMRI – which are complex, computationally expensive and difficult to analyse – on some key differences and similarities as compared to well-known MHD results.

Our main finding is that the KMRI at large amplitudes behaves quite similarly to the standard (MHD) MRI. In fact, in some cases – in particular, the MRI in a mean azimuthal–vertical field (also known as the magnetoviscous instability) – the MRI transitions from kinetic to MHD-like behaviour as its amplitude increases. Furthermore, in all cases studied we have seen the channel mode ($k_x = k_y = 0$ MRI mode) emerge as an approximate nonlinear solution of the kinetic equations at large amplitudes, in the same way as occurs in MHD (Goodman & Xu 1994). This is because the mirror-limited pressure anisotropy has the same form as the Lorentz force (since $\Delta p \propto B^2$), and this vanishes identically for an MRI channel mode. This points to an interesting robustness of the channel-mode solution in collisionless plasmas that had not been previously fully appreciated.

The similarity between the nonlinear physics of the KMRI and the MHD MRI is certainly not a given; for example, the nonlinear dynamics of shear Alfvén waves, which is related to the MRI (Balbus & Hawley 1998), differs very significantly between collisional and kinetic plasmas (Squire *et al.* 2016, 2017). Further, there remain a variety of 1-D nonlinear effects that cause modest differences when compared to standard MHD, and these could be important for the difficult task of designing and interpreting 3-D fully kinetic simulations. For example, depending on the level of overshoot of the pressure anisotropy above the mirror instability threshold (as would occur if there were insufficient scale separation between the large-scale dynamics and the gyro-scale; see § 6), the MRI mode may migrate to longer wavelengths at moderate amplitudes, or (in extreme cases) be completely stabilized. A more detailed overview of the most relevant 1-D results is given in § 3.4.

Motivated by the finding that there are no viable 1-D mechanisms for halting the growth of the kinetic MRI, as also found in previous numerical simulations (S06; Sharma *et al.* 2007, Riquelme *et al.* 2012, Kunz *et al.* 2014*b*, Hoshino 2015), we are left with the conclusion that 3-D effects must govern the collapse of a KMRI channel mode into a turbulent-like state. Following previous MHD studies (Goodman & Xu 1994; Latter *et al.* 2009; Pessah & Goodman 2009), we have considered 3-D mechanisms for mode saturation in terms of parasitic modes, secondary instabilities that feed off the large field and flow gradients of the channel mode, acting to disrupt it and cause its collapse into turbulence. Using both linear studies of parasitic modes and 3-D nonlinear simulations (with the modified ZEUS version of S06), we have found very little difference between the behaviour of parasitic modes in kinetic and MHD models. We have further shown that the observations of S06 of larger saturation amplitudes in kinetic models as compared to MHD may be straightforwardly explained by the migration of kinetic channel modes to longer wavelengths due to the mean pressure anisotropy (i.e. 1-D effects). This suggests that MHD results may be used

to give simple, zeroth-order estimates of the expected amplitude at which a KMRI channel mode should saturate into turbulence. Similar conclusions have also been found in global Braginskii MHD simulations of accretion disks (Foucart *et al.* 2017).

Although our results suggest that the breakdown into turbulence occurs in a similar way in kinetic theory and MHD, this does not necessarily imply that the saturated state of the turbulence is similar. Indeed, even following the pioneering 3-D nonlinear kinetic MRI simulations of Hoshino (2015) and Kunz *et al.* (2016), many properties of the saturated state of the KMRI – i.e. the turbulence – remain largely unknown. The zero-net-flux simulation of Kunz *et al.* (2016) found a level of turbulence that was comparable to high-Prandtl-number turbulence in MHD. However, there are some notable differences; for instance, a greater prevalence of coherent flows, and the fact that (in contrast to MHD) a large proportion of this transport arises from the pressure anisotropy directly. Some similar results were found in S06, Sharma *et al.* (2007) and Foucart *et al.* (2017) using fluid closures. However, these current results have explored only small regions of parameter space (e.g. the case of zero net flux), and it remains unknown how kinetic MRI turbulence relates (if at all) to MHD MRI turbulence. Both the strength of kinetic MRI turbulence and the different heating processes involved (in particular, the relative level of ion versus electron heating; Quataert 1998; Quataert & Gruzinov 1999), remain crucial unknowns in constraining phenomenological disk models.

Acknowledgements

Appendix A. Linear properties of the KMRI with a background azimuthal–vertical field

In this appendix, we derive various properties of the KMRI in the general case when the background field has a mixed-azimuthal–vertical configuration. We focus on modes with $k_x = k_y = 0$ as in §3.1.

A.1. *The fastest-growing wavenumber*

An important input to the nonlinear arguments put forth in §3.3 is the scaling of the fastest-growing wavenumber (and growth rate) with β_0. Our starting point is the Landau-fluid dispersion relation, obtained through the characteristic polynomial of the matrix resulting from the linearization of (2.1)–(2.7) (with $S/\Omega = 3/2$ and $\nu_c = 0$). We wish to find $k_{\max}$, the wavenumber that maximizes the growth rate $\gamma = \mathrm{Im}(\omega)$, as a function of $\beta_{0z} = 8\pi p_0/B_{0z}^2$ and $\alpha \equiv B_{0y}/B_{0z}$, assuming $\beta_{0z} \gg 1$ (because we consider only vertical modes, it is most straightforward to work with β_{0z} and v_{Az}, as opposed
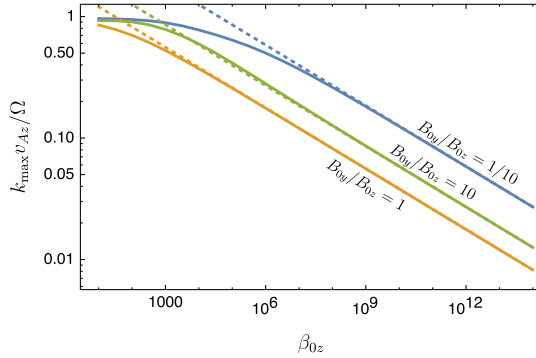
FIGURE 7. Scaling of k_{max}, the wavenumber of the fastest-growing mode, as a function of $\beta_{0z} = 8\pi p_0/B_{0z}^2$ for different choices of $\alpha \equiv B_{0y}/B_{0z}$. Solid lines show results from the numerical solution of the LF dispersion relation; dashed lines show the asymptotic result $k_{max}v_A/\Omega \sim \beta^{-1/6}$ (see (A 2)).

to quantities defined with $B_0^2 = B_{0y}^2 + B_{0z}^2$). Anticipating the scaling $k_{max}v_{Az}/\Omega \sim \beta_0^{-1/6}$, $\omega - \mathrm{i}\sqrt{3} \sim -\beta_0^{-1/3}$ we insert the ansatz $\beta_{0z} = \epsilon^{-6}\bar{\beta}_{0z}$, $k = \epsilon k_0 \bar{\beta}_{0z}^{-1/6}$, $\omega = \mathrm{i}\sqrt{3} + \mathrm{i}\epsilon^2\gamma^{(1)}$ and expand the resulting expression in ϵ. This yields the solution

$$\frac{\gamma}{\Omega} \approx \mathrm{i}\sqrt{3} + \gamma^{(1)} \approx \mathrm{i}\sqrt{3} - \frac{\alpha^2 k_0^3 + 12(1+\alpha^2)^{3/2}}{6\sqrt{\pi}\alpha^2 k_0 \beta_{0z}^{1/3}}, \qquad (A\,1)$$

which is an approximate KMRI dispersion relation, valid at high β near the peak growth rate. Maximizing (A 1) over k_0, we find,

$$\frac{k_{max}v_{Az}}{\Omega} \approx \left(\frac{12}{\pi\alpha}\right)^{1/6} \left(\frac{1}{\alpha} + \alpha\right)^{1/2} \beta_{0z}^{-1/6}, \qquad (A\,2)$$

and

$$\frac{\gamma_{max}}{\Omega} \approx \mathrm{i}\sqrt{3} - \frac{3^{5/6}}{(2\pi\alpha)^{1/3}} \left(\frac{1}{\alpha} + \alpha\right) \beta_{0z}^{-1/3}, \qquad (A\,3)$$

for the maximum growth rate, $\gamma_{max} = \gamma(k_{max})$.

Unsurprisingly (given that we carried out an expansion in $\beta_0^{-1/6}$) the expressions (A 2)–(A 3) are accurate only at very high β_0, particularly when $\alpha \neq 1$. A comparison with the true k_{max}, obtained by numerically maximizing the numerically computed dispersion relation, is illustrated in figure 7. We see that, very approximately, the asymptotic result (A 2) is valid when it predicts $k_{max}v_{Az}/\Omega \lesssim 1$ (as should be expected, since $k_{max}v_{Az}/\Omega \sim 1$ is the fastest-growing wavelength of the standard MRI). This suggests that the results (A 2) and (A 3) are applicable when $\beta_{0z} \gg (12/\pi)\alpha^{-4}$ for $\alpha \ll 1$, or when $\beta_{0z} \gg (12/\pi)\alpha^2$ for $\alpha \gg 1$. For β_{0z} lower than these estimates, k_{max} is less than the prediction (A 2) (there are also minor deviations above the prediction (A 2) when $\alpha > 1$, see figure 7). It is also worth noting that the dispersion relation around $k \approx k_{max}$ is not very strongly peaked (see, e.g. figure 1 in the main text). This implies that the fastest-growing mode grows only slightly faster than those with a similar wavelength, and it is unlikely to completely dominate by the time it reaches nonlinear amplitudes (see §§ 3.3 and 4.2).

A.2. *The fastest-growing mode*

The structure of the fastest-growing KMRI mode is also relevant to the nonlinear arguments of § 3.3. This can be found by inserting k_{max} and $\omega = \gamma_{max}$ into the matrix resulting from the linearization of (2.1)–(2.7), and solving for the amplitudes of each component δu_x, δB_x, etc., in terms of $\delta p_\perp$. To lowest order in β_{0z}^{-1}, this yields $\delta p_\parallel \approx -\alpha^2 \delta p_\perp$, as well as the following relations for the fastest-growing KMRI mode:

$$\frac{\delta B_x}{B_{0z}} \approx -\frac{1}{2}\left(\frac{1}{12\pi^2}\right)^{1/6}\frac{\alpha^2+1}{\alpha^{1/3}}\beta_{0z}^{2/3}\frac{\delta p_\perp}{p_0}, \qquad (A\,4)$$

$$\frac{\delta B_y}{B_{0z}} \approx \left(\frac{1}{12\pi^2}\right)^{1/3}\frac{(\alpha^2+1)^2}{\alpha^{5/3}}\beta_{0z}^{1/3}\frac{\delta p_\perp}{p_0}, \qquad (A\,5)$$

$$\frac{\delta u_x}{v_{Az}} \approx \frac{\mathrm{i}}{2}\left(\frac{3}{16\pi}\right)^{1/6}\alpha^{1/3}(\alpha^2+1)^{1/2}\beta_{0z}^{5/6}\frac{\delta p_\perp}{p_0}, \qquad (A\,6)$$

$$\frac{\delta u_y}{v_{Az}} \approx \frac{\mathrm{i}}{4}\left(\frac{81}{16\pi}\right)^{1/6}\alpha^{1/3}(\alpha^2+1)^{1/2}\beta_{0z}^{5/6}\frac{\delta p_\perp}{p_0}. \qquad (A\,7)$$

We see that $\delta B_x/B_0 \sim \beta_0^{1/3}\delta B_y/B_0$, *viz.,* the mode is dominated by the radial magnetic field.

A more intuitive way of understanding the structure of the KMRI mode is through the relations $\delta p_\perp/p_0 \approx \delta\rho/\rho_0 - \mathrm{i}\sqrt{\pi}\xi\delta B/B_0$, and $\delta p_\parallel/p_0 \approx \delta\rho/\rho_0 + \mathrm{i}\sqrt{\pi}\xi\delta B/B_0$, where $\xi = \omega/(\sqrt{2}\hat{\boldsymbol{b}}\cdot\boldsymbol{k}\,c_s)$ and $\delta B/B_0 = \delta B_y B_{0y}/B_0^2$ is the perturbation to the field strength. These relations are straightforwardly derived from the linear $\delta p_\perp$ and $\delta p_\parallel$ equations by balancing the production of pressure anisotropy against the smoothing action of the heat fluxes; see Q02. For $\alpha = B_{0y}/B_{0z} \approx 1$, these lead to (3.6), which is used in §§ 3.3 and 6 to estimate the amplitude at which the KMRI mode reaches the firehose and mirror limits (inserting k_{max}, one can also obtain (A 5)).

Appendix B. The form of the nonlinearity in growing KMRI modes

In this appendix, we derive, using asymptotic expansions, the form of the nonlinearity in growing KMRI modes. The method used is almost identical to that in the appendices of Squire *et al.* (2017), and the results are very similar, yielding few surprises. However, the results do serve to more formally justify some of the claims made in the main text, in particular those relating to the smoothing effects of the heat fluxes in §§ 2.3 and 3.2. They also allow one to explicitly calculate the form of the nonlinearity that causes the changes to KMRI-mode shape illustrated in figure 2.

We consider three cases – a double-adiabatic model, a collisionless LF model and a Braginskii MHD model – each with a purely vertical field (see §§ 3.2–3.2.2 and figure 2). While the double-adiabatic model is not considered in the main text (neglect of the heat fluxes is never a good approximation at high β), it provides a nice illustration of the importance of heat fluxes for high-β KMRI dynamics. We treat only the early nonlinear behaviour, that is, when pressure anisotropy first becomes important at low mode amplitudes. We also do not treat the $B_{0y} \neq 0$ KMRI (§ 3.3), since such modes stay close to linear until Δp reaches the firehose and mirror limits, at which point there are strong nonlinear modifications that cannot be captured with this type of asymptotic method (see figure 3).

B.1. *Equations and method*

Our method here is nearly identical to that used in Squire *et al.* (2017) to study shear-Alfvén waves, with only minor modifications to the equations to account for the rotation and shear flow. We consider a mode of wavelength $2\pi/k_\parallel$ in a background plasma with density ρ_0, thermal pressure p_0, and vertical magnetic field $\boldsymbol{B}_0 = B_0\hat{\boldsymbol{z}}$. For simplicity, we normalize length scales to $k_\parallel^{-1}$, velocities to $v_{A0} \equiv B_0/\sqrt{4\pi\rho_0}$, time scales to $\omega_A^{-1} \equiv (k_\parallel v_{A0})^{-1}$, densities to ρ_0, pressures to p_0 and magnetic fields to B_0. Splitting the velocity $\boldsymbol{u}$ into its equilibrium ($\boldsymbol{U}_0 = -Sx\hat{\boldsymbol{y}}$) and fluctuating ($\delta\boldsymbol{u}$) parts, equations (2.1)–(2.7) become, respectively,

$$\frac{\mathrm{d}\rho}{\mathrm{d}t} = -\rho\boldsymbol{\nabla}\cdot\delta\boldsymbol{u}, \tag{B 1}$$

$$\rho\left(\frac{\mathrm{d}\delta\boldsymbol{u}}{\mathrm{d}t} + 2\overline{\Omega}\hat{\boldsymbol{z}}\times\delta\boldsymbol{u} - \overline{S}\delta u_x\hat{\boldsymbol{y}}\right) = -\boldsymbol{\nabla}\left(\frac{\beta_0}{2}p_\perp + \frac{B^2}{2}\right) + \boldsymbol{\nabla}\cdot\left[\hat{\boldsymbol{b}}\hat{\boldsymbol{b}}\left(\frac{\beta_0}{2}\Delta + B^2\right)\right], \tag{B 2}$$

$$\frac{\mathrm{d}\boldsymbol{B}}{\mathrm{d}t} + \overline{S}B_x\hat{\boldsymbol{y}} = \boldsymbol{B}\cdot\boldsymbol{\nabla}\delta\boldsymbol{u} - \boldsymbol{B}\boldsymbol{\nabla}\cdot\delta\boldsymbol{u}, \tag{B 3}$$

$$\frac{\mathrm{d}p_\perp}{\mathrm{d}t} + p_\perp\hat{b}_x\hat{b}_y\overline{S} = -\beta_0^{1/2}[\boldsymbol{\nabla}\cdot(q_\perp\hat{\boldsymbol{b}}) + q_\perp\boldsymbol{\nabla}\cdot\hat{\boldsymbol{b}}] + p_\perp\hat{\boldsymbol{b}}\hat{\boldsymbol{b}}:\boldsymbol{\nabla}\delta\boldsymbol{u} - 2p_\perp\boldsymbol{\nabla}\cdot\delta\boldsymbol{u} - \overline{v}_c\Delta, \tag{B 4}$$

$$\frac{\mathrm{d}p_\parallel}{\mathrm{d}t} - 2p_\parallel\hat{b}_x\hat{b}_y\overline{S} = -\beta_0^{1/2}[\boldsymbol{\nabla}\cdot(q_\parallel\hat{\boldsymbol{b}}) - 2q_\perp\boldsymbol{\nabla}\cdot\hat{\boldsymbol{b}}] - 2p_\parallel\hat{\boldsymbol{b}}\hat{\boldsymbol{b}}:\boldsymbol{\nabla}\delta\boldsymbol{u} - p_\parallel\boldsymbol{\nabla}\cdot\delta\boldsymbol{u} + 2\overline{v}_c\Delta, \tag{B 5}$$

$$q_\perp = -\sqrt{\frac{p_\parallel}{\pi\rho}}\frac{1}{|k_\parallel| + \overline{v}_c(\beta_0\pi p_\parallel/\rho)^{-1/2}}\left[\rho\boldsymbol{\nabla}_\parallel\left(\frac{p_\perp}{\rho}\right) - p_\perp\left(1 - \frac{p_\perp}{p_\parallel}\right)\frac{\boldsymbol{\nabla}_\parallel B}{B}\right], \tag{B 6}$$

$$q_\parallel = -2\sqrt{\frac{p_\parallel}{\pi\rho}}\frac{1}{|k_\parallel| + (3\pi/2 - 4)\overline{v}_c(\beta_0\pi p_\parallel/\rho)^{-1/2}}\rho\boldsymbol{\nabla}_\parallel\left(\frac{p_\parallel}{\rho}\right), \tag{B 7}$$

where $\overline{v}_c \equiv v_c/\omega_A$ and $\overline{\Omega} \equiv \Omega/\omega_A$. The heat fluxes $q_{\perp,\parallel}$ are normalized using the sound speed $c_s \equiv \beta_0^{1/2}v_{A0} = \sqrt{2p_0/\rho_0}$ (note that we have changed the definition of c_s from the main text here, so as to remove various inconvenient factors of 2 from (B 1)–(B 7)). As in the main text, $\Delta \equiv p_\perp - p_\parallel$ denotes the dimensionless pressure anisotropy, $\beta_0 \equiv 8\pi p_0/B_0^2$, and

$$\frac{\mathrm{d}}{\mathrm{d}t} = \frac{\partial}{\partial t} - \overline{S}x\frac{\partial}{\partial y} + \delta\boldsymbol{u}\cdot\boldsymbol{\nabla} \tag{B 8}$$

is the convective derivative.

Following § 3.2, we focus on the nonlinear evolution of a 1-D (in z) channel mode. This involves an asymptotic expansion of (B 1)–(B 7), which is constructed as follows. Figure 1 shows that the $k_\parallel = k_z$ KMRI mode grows fastest for $k_\parallel v_A/\Omega \sim 1$, and so we order $\overline{\Omega} \sim 1$. Following Squire *et al.* (2017), we order the (dimensionless) MRI-mode amplitude $\delta\boldsymbol{B}_\perp \sim \delta\boldsymbol{u}_\perp \sim \epsilon \ll 1$ and the equilibrium plasma beta parameter β_0 such that the effect of the pressure anisotropy Δ is as important as that of the linear terms, *viz.*, $\beta_0\Delta \sim 1$. Because the growth rate of the fastest-growing MRI mode is $\gamma \sim \Omega \sim \omega_A$, we order the (dimensionless) spatial and temporal derivatives to be $\sim O(1)$. This ordering captures nonlinear effects on the MRI mode just before it drives the pressure anisotropy to the mirror limit $\beta_0\Delta \approx 1$, in both the collisionless and weakly collisional (Braginskii) cases.

In what follows, we use $\langle f \rangle$ to denote a spatial (z) average of some function f and $\widetilde{f} \equiv f - \langle f \rangle$ to denote the spatially varying part of f.

B.2. *Collisionless limit: double-adiabatic closure*

Because the pressure anisotropy is generated proportional to the change in B, in the double-adiabatic case Δ scales as $\sim \delta B_\perp^2$. Thus we order $\beta_0 \sim \epsilon^{-2}$. The ordering of all variables is then as follows (cf. Squire *et al.* 2017):

$$\boldsymbol{u}_\perp = -\overline{S}x\hat{\boldsymbol{y}} + \epsilon\,\delta\boldsymbol{u}_{\perp 1} + \epsilon^2\,\delta\boldsymbol{u}_{\perp 2} + \cdots, \tag{B 9a}$$

$$u_z = 0 + 0 + \epsilon^2\,\delta u_{z2} + \epsilon^3\,\delta u_{z3} + \cdots \tag{B 9b}$$

$$\boldsymbol{B}_\perp = 0 + \epsilon\,\delta\boldsymbol{B}_{\perp 1} + \epsilon^2\,\delta\boldsymbol{B}_{\perp 2} + \cdots, \tag{B 9c}$$

$$\rho = 1 + 0 + \epsilon^2\,\delta\rho_2 + \epsilon^3\,\delta\rho_3 + \cdots, \tag{B 9d}$$

$$p_\perp = 1 + 0 + \epsilon^2\,\delta p_{\perp 2} + \epsilon^3\,\delta p_{\perp 3} + \cdots, \tag{B 9e}$$

$$p_\parallel = 1 + 0 + \epsilon^2\,\delta p_{\parallel 2} + \epsilon^3\,\delta p_{\parallel 3} + \cdots, \tag{B 9f}$$

where the numerical subscripts denote the order in ϵ. Equations (B 9a)–(B 9f) are inserted into the MRI equations (B 1)–(B 5) with $q_\perp = q_\parallel = 0$ and the result is examined order by order in ϵ.

Order ϵ^0. Only the z component of (B 2) contributes at this order, giving $\partial_z \delta p_{\parallel 2} = 0$ or $\widetilde{\delta p_{\parallel 2}} = 0$. This condition expresses parallel pressure balance.

Order ϵ^1. The parallel component of the momentum equation (B 2) gives $\widetilde{\delta p_{\parallel 3}} = 0$. The perpendicular components of the momentum and induction equations (B 2)–(B 3) provide evolution equations for the linear MRI:

$$\partial_t \delta\boldsymbol{u}_{\perp 1} + 2\overline{\Omega}\hat{\boldsymbol{z}} \times \delta\boldsymbol{u}_{\perp 1} - \overline{S}\delta u_{x1}\hat{\boldsymbol{y}} = \partial_z\left[\delta\boldsymbol{B}_{\perp 1}\left(1 + \frac{\beta_0}{2}\Delta_2\right)\right], \tag{B 10}$$

$$\partial_t \delta\boldsymbol{B}_{\perp 1} + \overline{S}\delta B_{x1}\hat{\boldsymbol{y}} = \partial_z \delta\boldsymbol{u}_{\perp 1}. \tag{B 11}$$

To close this system, we require $\Delta_2 = \delta p_{\perp 2} - \delta p_{\parallel 2}$ as a function of $\delta\boldsymbol{u}_{\perp 2}$ and $\delta\boldsymbol{B}_{\perp 2}$, which is obtained at next order.

Order ϵ^2. At this order, we require only the pressure equations (B 4)–(B 5) to obtain Δ_2 for use in (B 10). Expanding $\hat{\boldsymbol{b}}\hat{\boldsymbol{b}} : \boldsymbol{\nabla}\delta\boldsymbol{u} = \hat{b}_z^2\partial_z\delta u_z + \hat{\boldsymbol{b}}\hat{\boldsymbol{b}} : \boldsymbol{\nabla}\delta\boldsymbol{u}_\perp$, equations (B 4)–(B 5) become

$$\partial_t \delta p_{\perp 2} + \partial_z \delta u_{z2} = \delta\boldsymbol{B}_{\perp 1} \cdot \partial_z \delta\boldsymbol{u}_{\perp 1} - \overline{S}\delta B_{x1}\delta B_{y1} = \tfrac{1}{2}\partial_t \delta B_{\perp 1}^2, \tag{B 12}$$

$$\partial_t \delta p_{\parallel 2} + 3\partial_z \delta u_{z2} = -2\delta\boldsymbol{B}_{\perp 1} \cdot \partial_z \delta\boldsymbol{u}_{\perp 1} + 2\overline{S}\delta B_{x1}\delta B_{y1} = -\partial_t \delta B_{\perp 1}^2, \tag{B 13}$$

where $\delta B_{\perp 1}^2 \equiv \delta B_{x1}^2 + \delta B_{y1}^2$; the final equalities in these equations follow from (B 11). We can then solve for $\partial_z \delta u_{z2} = \widetilde{\partial_z \delta u_{z2}}$ using (B 13) and insert this into (B 12) to find

$$\partial_t \Delta_2 = \tfrac{5}{6}\partial_t \delta B_{\perp 1}^2 + \tfrac{2}{3}\partial_t \langle \delta B_{\perp 1}^2 \rangle. \tag{B 14}$$

If we then assume that the mode starts growing from vanishingly small initial conditions, equation (B 14) may be straightforwardly integrated to obtain

$$\Delta_2 = \tfrac{5}{6}\delta B_{\perp 1}^2 + \tfrac{2}{3}\langle \delta B_{\perp 1}^2 \rangle. \tag{B 15}$$

This expression may be inserted into (B 10) to yield a simple nonlinear equation for the growing MRI mode:

$$\partial_t^2 \delta \boldsymbol{B}_{\perp 1} + 2\overline{\Omega}\hat{z} \times \partial_t \delta \boldsymbol{B}_{\perp 1} - 2\overline{S\Omega}\delta B_{x1}\hat{x}$$
$$= \partial_z^2 \left\{ \delta \boldsymbol{B}_{\perp 1} \left[1 + \frac{\beta_0}{2}\left(\frac{5}{6}\delta B_{\perp 1}^2 + \frac{2}{3}\langle \delta B_{\perp 1}^2 \rangle \right) \right] \right\}, \tag{B 16}$$

where we have grouped all nonlinear terms on the right-hand side.

This rather simple expression of Δ_2 (B 15) arises because, while parallel pressure balance enforces $\partial_z \delta p_\parallel \approx 0$ in the growing mode, there is no equivalent pressure balance condition for $\delta p_\perp$. The same result can also be obtained by projecting the driving of Δp due to the MRI mode onto the eigenmodes of the double-adiabatic equations; this agrees with 1-D nonlinear simulations (not shown). Because the spatial variation in the anisotropy is comparable to its mean (i.e. $\langle \Delta_2 \rangle \sim \widetilde{\Delta_2}$) the double-adiabatic model will cause nonlinear modifications to the mode shape as it approaches the mirror limit (similar to the Braginskii model; see figure 2(*c*) and § B.4).

B.3. *Collisionless: Landau-fluid closure*

In this section, we repeat the calculation detailed in § B.2 but include the heat fluxes $q_\perp$ (B 6) and $q_\parallel$ (B 7) with $\overline{\nu}_c = 0$. In a high-β plasma with Alfvénic fluctuations, such flows rapidly smooth pressure perturbations and, as a result, lead to a Δ_2 that is smooth, *viz.*, $\widetilde{\Delta_2} = 0$. The ordering is the same as that used in the double-adiabatic case (§ B.2), but with the addition of the heat fluxes,

$$q_\perp = \epsilon^2 \frac{1}{\sqrt{\pi}}\frac{\partial_z}{|k_z|}(\delta p_{\perp 2} - \delta \rho_2) + \epsilon^3 \frac{1}{\sqrt{\pi}}\frac{\partial_z}{|k_z|}(\delta p_{\perp 3} - \delta \rho_3) + O(\epsilon^4), \tag{B 17}$$

$$q_\parallel = \epsilon^2 \frac{2}{\sqrt{\pi}}\frac{\partial_z}{|k_z|}(\delta p_{\parallel 2} - \delta \rho_2) + \epsilon^3 \frac{2}{\sqrt{\pi}}\frac{\partial_z}{|k_z|}(\delta p_{\parallel 3} - \delta \rho_3) + O(\epsilon^4). \tag{B 18}$$

The $\nabla \cdot (q_{\perp,\parallel}\hat{\boldsymbol{b}})$ contributions to the pressure equations (B 4)–(B 5) then simplify to $\epsilon^2 \partial_z q_{\perp,\parallel 2} + \epsilon^3 \partial_z q_{\perp,\parallel 3} + O(\epsilon^4)$, i.e. heat flows along $\boldsymbol{B}_0 = \hat{z}$ to lowest order.

The equations up to order ϵ^1 are identical to those found in § B.2, aside from additional contributions from the $\nabla \cdot (q_{\perp,\parallel}\hat{\boldsymbol{b}})$ terms in the pressure equations (B 4)–(B 5), namely,

$$\pi^{-1/2}\beta_0^{1/2}|k_z|(\delta p_{\perp 2} - \delta \rho_2) = 0, \tag{B 19}$$
$$2\pi^{-1/2}\beta_0^{1/2}|k_z|(\delta p_{\parallel 2} - \delta \rho_2) = 0, \tag{B 20}$$

where we have used $\partial_z^2/|k_z| = -|k_z|$ to simplify the non-local diffusion operators. Combining (B 19)–(B 20) with the continuity equation (B 1) and parallel pressure balance $\widetilde{\delta p_{\parallel 2}} = 0$, we obtain

$$\widetilde{\delta p_{\perp 2}} = \widetilde{\delta \rho_2} = \widetilde{\delta u_{z2}} = \widetilde{\Delta_2} = 0. \tag{B 21}$$

This formally justifies the statements in §§ 3.2 and 2.3 that Δ is spatially constant to lowest order.

At order ϵ^2, the pressure equations (B 4)–(B 5) are

$$\partial_t \delta p_{\perp 2} + \partial_z \delta u_{z2} + \pi^{-1/2} \beta_0^{1/2} |k_z| (\delta p_{\perp 3} - \delta \rho_3) = \tfrac{1}{2} \partial_t \delta B_{\perp 1}^2, \tag{B 22}$$

$$\partial_t \delta p_{\parallel 2} + 3 \partial_z \delta u_{z2} + 2 \pi^{-1/2} \beta_0^{1/2} |k_z| (\delta p_{\parallel 3} - \delta \rho_3) = -\partial_t \delta B_{\perp 1}^2. \tag{B 23}$$

Spatially averaging these equations, using $\widetilde{\delta p_{\perp 2}} = \widetilde{\delta p_{\parallel 2}} = 0$, and again assuming that the mode growth starts from negligibly small amplitudes (i.e. $\delta B_{\perp 1}^2(t = 0) = 0$), we find

$$\Delta_2 = \tfrac{3}{2} \langle \delta B_{\perp 1}^2 \rangle. \tag{B 24}$$

This can be inserted into (B 10)–(B 11) to obtain the following evolution equation for $\delta \boldsymbol{B}_{\perp 1}$:

$$\partial_t^2 \delta \boldsymbol{B}_{\perp 1} + 2 \overline{\Omega} \hat{\boldsymbol{z}} \times \partial_t \delta \boldsymbol{B}_{\perp 1} - 2 \overline{S \Omega} \, \delta B_{x1} \hat{\boldsymbol{x}} = \partial_z^2 \left[\delta \boldsymbol{B}_{\perp 1} \left(1 + \frac{3 \beta_0}{4} \langle \delta B_{\perp 1}^2 \rangle \right) \right], \tag{B 25}$$

which remains valid until Δ_2 exceeds the mirror threshold (at which point its growth should be limited by the unresolved mirror instability, as discussed in § 3.2).

As expected, the presence of such strong heat fluxes has rendered the KMRI equations (B 10)–(B 11) much simpler than in the double-adiabatic case.[13] Physically, the spatial average inside the nonlinear term in (B 25) implies that, if a KMRI mode is initially sinusoidal, it will remain so even as it becomes nonlinear (see figure 2*b* for a demonstration of this property). We can then use (B 25) to write down an ordinary differential equation for the amplitude evolution of a single MRI mode $\delta \boldsymbol{B}_\perp = \delta \boldsymbol{B}_\perp(t) \mathrm{e}^{\mathrm{i} k_\parallel z}$, $\delta \boldsymbol{u}_\perp = \delta \boldsymbol{u}_\perp(t) \mathrm{e}^{\mathrm{i} k_\parallel z}$:

$$\frac{\mathrm{d}^2 \delta \boldsymbol{B}_{\perp 1}}{\mathrm{d} t^2} + 2 \overline{\Omega} \hat{\boldsymbol{z}} \times \frac{\mathrm{d} \delta \boldsymbol{B}_{\perp 1}}{\mathrm{d} t} - 2 \overline{S \Omega} \, \delta B_{x1} \hat{\boldsymbol{x}} = -k_\parallel^2 \delta \boldsymbol{B}_{\perp 1} \left(1 + \frac{3 \beta_0}{8} \delta B_{\perp 1}^2 \right), \tag{B 26}$$

$$\delta \boldsymbol{u}_{\perp 1} = -\frac{\mathrm{i}}{k_\parallel} \left(\frac{\mathrm{d} \delta \boldsymbol{B}_{\perp 1}}{\mathrm{d} t} + \overline{S} \delta B_{x1} \hat{\boldsymbol{y}} \right), \tag{B 27}$$

where we have used $\langle \sin^2(k_\parallel z) \rangle = 1/2$. Solutions to (B 26)–(B 27) correctly reproduce the change in relative amplitudes of $\delta \boldsymbol{B}_\perp$ and $\delta \boldsymbol{u}_\perp$ as seen in figure 2(*b*) (e.g. the relative increase in δu_y and relative decrease of δu_x). Of course, if there is more than one growing mode, the pressure-anisotropy nonlinearity (B 24) does couple the modes, which could allow, for example, a larger-wavelength mode to 'take over' due to the positive pressure anisotropy (see § 3.2).

If one were so inclined, a continuation of the expansion to $O(\epsilon^3)$ would yield equations for the spatial variation in Δ. However, because the expected effect on the mode is very small for $\beta_0 \gg 1$, we do not do this here (see, e.g. appendix A.3.1 of Squire *et al.* 2017).

B.4. *Weakly collisional: Braginskii closure*

In this section, we treat the weakly collisional, Braginskii MHD limit. As discussed in §§ 2 and 3.2.2, 3.3.2, the Braginskii regime is relevant when $\overline{\nu}_c \equiv \nu_c / \omega_A \sim \nu_c / \Omega \gg 1$, with the corrections to the MRI due to pressure anisotropy becoming unimportant

---

[13]Interestingly, a similar saturation mechanism also arises for the standard (MHD) MRI in a non-periodic system when it is near the marginal stability condition (Vasil 2015).

when $\overline{\nu}_c \gtrsim \beta$ (see Sharma *et al.* 2003). Within the relevant range $1 \ll \overline{\nu}_c \ll \beta$, one may obtain a variety of behaviours depending upon whether or not the heat fluxes play a significant role in the evolution of Δp. If $\overline{\nu}_c \gg \beta^{1/2}$, the heat fluxes are suppressed by the collisionality and do not strongly influence Δp; if instead $\overline{\nu}_c \lesssim \beta^{1/2}$, the heat fluxes smooth Δp in space[14] on a time scale shorter than that over which Δp is produced by the changing B (see Squire *et al.* 2017 for further discussion). We present here only the former limit ($\overline{\nu}_c \gg \beta^{1/2}$), which leads to the closure used in the main text, equation (2.8); in the $\overline{\nu}_c \ll \beta^{1/2}$ limit, the heat fluxes smooth out Δp near the nodes of δB and so Δp is almost spatially constant as the mirror limit is approach (see the discussion in § 3.2.2). In the intermediate case $\overline{\nu}_c \sim \beta^{1/2}$, a valid closure for Δp has been obtained by Squire *et al.* (2017) – see their equations (B12)–(B15).

The ordering introduced above, $\delta \boldsymbol{B}_\perp \sim \delta \boldsymbol{u}_\perp \sim \epsilon$ with $\beta_0 \Delta \sim 1$, coupled with the Braginskii pressure anisotropy $\Delta \sim \overline{\nu}_c^{-1} \mathrm{d} \ln B / \mathrm{d}t$, suggests that we order $\overline{\nu}_c \sim \epsilon^2 \beta_0$. The simultaneous requirement that $\overline{\nu}_c \gg \beta_0^{1/2}$ for the 'high-collisionality' regime where heat fluxes are collisionally suppressed then implies the ordering $\overline{\nu}_c \sim O(\epsilon^{-4})$, $\beta_0 \sim O(\epsilon^{-6})$. For the other variables, we adopt the orderings $p_\perp \sim p_\parallel \sim \rho \sim 1 + O(\epsilon^6)$ and $\delta u_z \sim O(\epsilon^6)$. The $O(1)$ and $O(\epsilon)$ equations are then almost the same as in § B.2: the parallel momentum equation gives $\partial_z \delta p_{\parallel 6} = 0$, and the perpendicular momentum and induction equations are identical to (B 10)–(B 11) but with Δ_2 replaced by Δ_6. At $O(\epsilon^2)$, the pressure equations (B 4) and (B 5) may be combined to give

$$\overline{\nu}_c \Delta_6 = \delta \boldsymbol{B}_{\perp 1} \cdot \partial_z \delta \boldsymbol{u}_{\perp 1} - \overline{S} \delta B_{x1} \delta B_{y1} = \tfrac{1}{2} \partial_t \delta B_{\perp 1}^2; \qquad (B\,28)$$

the heat-flux terms appear at $O(\epsilon^4)$. This is exactly as was anticipated (cf. (2.8)). The nonlinear equation for the growing mode is then simply

$$\partial_t^2 \delta \boldsymbol{B}_{\perp 1} + 2\overline{\Omega} \hat{\boldsymbol{z}} \times \partial_t \delta \boldsymbol{B}_{\perp 1} - 2\overline{S\Omega}\, \delta B_{x1} \hat{\boldsymbol{x}} = \partial_z^2 \left[\delta \boldsymbol{B}_{\perp 1} \left(1 + \frac{\beta_0}{4\overline{\nu}_c} \partial_t \delta B_{\perp 1}^2 \right) \right]. \qquad (B\,29)$$

Because the nonlinearity in (B 29) depends on $\delta B_{\perp 1}^2(z)$ (rather than $\langle \delta B_{\perp 1}^2 \rangle$), it will distort the shape of an initially sinusoidal mode, as discussed in § 3.2.2 and exhibited in figure 2(*c*). Thus, we cannot reduce (B 29) to an ordinary differential equation for a single mode, as in the collisionless (LF) derivation (see (B 26)).

REFERENCES

BALBUS, S. A. 2004 Viscous shear instability in weakly magnetized, dilute plasmas. *Astrophys. J.* **616** (2), 857–864.

BALBUS, S. A. & HAWLEY, J. F. 1991 A powerful local shear instability in weakly magnetized disks. I – linear analysis. II – nonlinear evolution. *Astrophys. J.* **376**, 214–233.

BALBUS, S. A. & HAWLEY, J. F. 1992 A powerful local shear instability in weakly magnetized disks. IV. Nonaxisymmetric perturbations. *Astrophys. J.* **400**, 610–621.

BALBUS, S. A. & HAWLEY, J. F. 1998 Instability, turbulence, and enhanced transport in accretion disks. *Rev. Mod. Phys.* **70** (1), 1.

BALE, S. D., KASPER, J. C., HOWES, G. G., QUATAERT, E., SALEM, C. & SUNDKVIST, D. 2009 Magnetic fluctuation power near proton temperature anisotropy instability thresholds in the solar wind. *Phys. Rev. Lett.* **103** (2), 211101.

[14]Specifically, the relative magnitude of the rate of heat-flux smoothing of Δp compared to its rate of creation (via $\mathrm{d} \ln B / \mathrm{d}t$) varies between $\beta^{1/2}$ (as in the collisionless case), when $\overline{\nu}_c \ll \beta^{1/2}$, and 1, when $\overline{\nu}_c \sim \beta^{1/2}$.

BLACKMAN, E. G. 2012 Accretion disks and dynamos: toward a unified mean field theory. *Phys. Scr.* **86** (5), 058202.

BODO, G., MIGNONE, A., CATTANEO, F., ROSSI, P. & FERRARI, A. 2008 Aspect ratio dependence in magnetorotational instability shearing box simulations. *Astron. Astrophys.* **487** (1), 1–5.

BRAGINSKII, S. I. 1965 Transport processes in a plasma. *Rev. Plasma Phys.* **1**, 205.

CHANDRA, M., GAMMIE, C. F., FOUCART, F. & QUATAERT, E. 2015 An extended magnetohydrodynamics model for relativistic weakly collisional plasmas. *Astrophys. J.* **810** (2), 162.

CHANDRASEKHAR, S., KAUFMAN, A. N. & WATSON, K. M. 1958 The stability of the pinch. *Proc. R. Soc. Lond.* A **245**, 435–455.

CHEW, C. F., GOLDBERGER, M. L. & LOW, F. E. 1956 *Proc. R. Soc. Lond.* A **236**, 112.

DAVIDSON, R. C. & VÖLK, H. J. 1968 Macroscopic quasilinear theory of the garden-hose instability. *Phys. Fluids* **11**, 2259–2264.

FERRARO, N. M. 2007 Finite Larmor radius effects on the magnetorotational instability. *Astrophys. J.* **662** (1), 512–516.

FOUCART, F., CHANDRA, M., GAMMIE, C. F. & QUATAERT, E. 2015 Evolution of accretion discs around a Kerr black hole using extended magnetohydrodynamics. *Mon. Not. R. Astron. Soc.* **456** (2), 1332–1345.

FOUCART, F., CHANDRA, M., GAMMIE, C. F., QUATAERT, E. & TCHEKHOVSKOY, A. 2017 How important is non-ideal physics in simulations of sub-Eddington accretion on to spinning black holes? *Mon. Not. R. Astron. Soc.* **470**, 2240–2252.

FROMANG, S., PAPALOIZOU, J., LESUR, G. & HEINEMANN, T. 2007 MHD simulations of the magnetorotational instability in a shearing box with zero net flux. II. The effect of transport coefficients. *Astron. Astrophys.* **476** (3), 1123–1132.

FROMANG, S. & STONE, J. M. 2009 Turbulent resistivity driven by the magnetorotational instability. *Astron. Astrophys.* **507** (1), 19–28.

GARY, S. P., MCKEAN, M. E. & WINSKE, D. 1993 Ion cyclotron anisotropy instabilities in the magnetosheath – theory and simulations. *J. Geophys. Res.* **98**, 3963–3971.

GARY, S. P., WANG, J., WINSKE, D. & FUSELIER, S. A. 1997 Proton temperature anisotropy upper bound. *J. Geophys. Res.* **102** (A), 27159–27170.

GOODMAN, J. & XU, G. 1994 Parasitic instabilities in magnetized, differentially rotating disks. *Astrophys. J.* **432**, 213–223.

HAMMETT, G. W., DORLAND, W. & PERKINS, F. W. 1992 Fluid models of phase mixing, Landau damping, and nonlinear gyrokinetic dynamics. *Phys. Fluids* B **4**, 2052–2061.

HAMMETT, G. W. & PERKINS, F. W. 1990 Fluid moment models for Landau damping with application to the ion-temperature-gradient instability. *Phys. Rev. Lett.* **64**, 3019–3022.

HASEGAWA, A. 1969 Drift mirror instability of the magnetosphere. *Phys. Fluids* **12**, 2642–2650.

HAWLEY, J. F. & BALBUS, S. A. 2002 The dynamical structure of nonradiative black hole accretion flows. *Astrophys. J.* **573**, 738–748.

HAWLEY, J. F., BALBUS, S. A. & STONE, J. M. 2001 A magnetohydrodynamic nonradiative accretion flow in three dimensions. *Astrophys. J.* **554**, L49–L52.

HAWLEY, J. F., GAMMIE, C. F. & BALBUS, S. A. 1995 Local three-dimensional magnetohydrodynamic simulations of accretion disks. *Astrophys. J.* **440**, 742.

HEINEMANN, T. & QUATAERT, E. 2014 Linear Vlasov theory in the shearing sheet approximation with application to the magneto-rotational instability. *Astrophys. J.* **792** (1), 70.

HELLINGER, P. 2007 Comment on the linear mirror instability near the threshold. *Phys. Plasmas* **14** (8), 082105.

HELLINGER, P. & MATSUMOTO, H. 2000 New kinetic instability: Oblique Alfvén firehose. *J. Geophys. Res.* **105** (A), 10519–10526.

HELLINGER, P., MATTEINI, L., LANDI, S., VERDINI, A., FRANCI, L. & TRÁVNÍČEK, P. M. 2015 Plasma turbulence and kinetic instabilities at ion scales in the expanding solar wind. *Astrophys. J.* **811** (2), L32.

HELLINGER, P. & TRÁVNÍČEK, P. M. 2008 Oblique proton fire hose instability in the expanding solar wind: hybrid simulations. *J. Geophys. Res.* **113**, A10.

HOSHINO, M. 2013 Particle acceleration during magnetorotational instability in a collisionless accretion disk. *Astrophys. J.* **773**, 118.

HOSHINO, M. 2015 Angular momentum transport and particle acceleration during magnetorotational instability in a kinetic accretion disk. *Phys. Rev. Lett.* **114** (6), 061101.

JOHNSON, B. M. 2007 Magnetohydrodynamic shearing waves. *Astrophys. J.* **660** (2), 1375.

KASPER, J. C., LAZARUS, A. J. & GARY, S. P. 2002 Wind/SWE observations of firehose constraint on solar wind proton temperature anisotropy. *Geophys. Res. Lett.* **29** (1), 1839-1.

KIM, H. P., HWANG, J., SEOUGH, J. J. & YOON, P. H. 2017 Electron temperature anisotropy regulation by whistler instability. *J. Geophys. Res.* **122**, 4410–4419.

KLEIN, K. G. & HOWES, G. G. 2015 Predicted impacts of proton temperature anisotropy on solar wind turbulence. *Phys. Plasmas* **22** (3), 032903.

KOMAROV, S. V., CHURAZOV, E. M., KUNZ, M. W. & SCHEKOCHIHIN, A. A. 2016 Thermal conduction in a mirror-unstable plasma. *Mon. Not. R. Astron. Soc.* **460**, 467–477.

KOWAL, G., FALCETA-GONÇALVES, D. A. & LAZARIAN, A. 2011 Turbulence in collisionless plasmas: statistical analysis from numerical simulations with pressure anisotropy. *New J. Phys.* **13** (5), 053001.

KULSRUD, R. M. 1983 MHD description of a plasma. In *Handbook of Plasma Physics* (ed. M. N. Rosenbluth & R. Z. Sagdeev), vol. 1, p. 115. North Holland.

KUNZ, M. W., SCHEKOCHIHIN, A. A., CHEN, C. H. K., ABEL, I. G. & COWLEY, S. C. 2015 Inertial-range kinetic turbulence in pressure-anisotropic astrophysical plasmas. *J. Plasma Phys.* **81** (5), 325810501.

KUNZ, M. W., SCHEKOCHIHIN, A. A. & STONE, J. M. 2014a Firehose and mirror instabilities in a collisionless shearing plasma. *Phys. Rev. Lett.* **112** (2), 205003.

KUNZ, M. W., STONE, J. M. & BAI, X.-N. 2014b Pegasus: a new hybrid-kinetic particle-in-cell code for astrophysical plasma dynamics. *J. Comput. Phys.* **259**, 154–174.

KUNZ, M. W., STONE, J. M. & QUATAERT, E. 2016 Magnetorotational turbulence and dynamo in a collisionless plasma. *Phys. Rev. Lett.* **117** (2), 235101.

LATTER, H. N., FROMANG, S. & GRESSEL, O. 2010 MRI channel flows in vertically stratified models of accretion discs. *Mon. Not. R. Astron. Soc.* **406** (2), 848–862.

LATTER, H. N., LESAFFRE, P. & BALBUS, S. A. 2009 MRI channel flows and their parasites. *Mon. Not. R. Astron. Soc.* **394** (2), 715–729.

LESUR, G. & LONGARETTI, P. Y. 2007 Impact of dimensionless numbers on the efficiency of magnetorotational instability induced turbulent transport. *Mon. Not. R. Astron. Soc.* **378** (4), 1471–1480.

LONGARETTI, P. Y. & LESUR, G. 2010 MRI-driven turbulent transport: the role of dissipation, channel modes and their parasites. *Astron. Astrophys.* **516**, 51.

MEHEUT, H., FROMANG, S., LESUR, G., JOOS, M. & LONGARETTI, P.-Y. 2015 Angular momentum transport and large eddy simulations in magnetorotational turbulence: the small Pm limit. *Astron. Astrophys.* **579**, A117.

MELVILLE, S., SCHEKOCHIHIN, A. A. & KUNZ, M. W. 2016 Pressure-anisotropy-driven microturbulence and magnetic-field evolution in shearing, collisionless plasma. *Mon. Not. R. Astron. Soc.* **459** (3), 2701–2720.

MIKHAILOVSKII, A. B. & TSYPIN, V. S. 1971 Transport equations and gradient instabilities in a high pressure collisional plasma. *Plasma Phys.* **13**, 785–798.

MOGAVERO, F. & SCHEKOCHIHIN, A. A. 2014 Models of magnetic field evolution and effective viscosity in weakly collisional extragalactic plasmas. *Mon. Not. R. Astron. Soc.* **440** (4), 3226–3242.

NARAYAN, R., MAHADEVAN, R. & QUATAERT, E. 1998 Advection-dominated accretion around black holes. In *Theory of Black Hole Accretion Disks* (ed. M. A. Abramowicz, G. Björnsson & J. E. Pringle), pp. 148–182.

PARKER, E. N. 1958 Dynamical instability in an anisotropic ionized gas of low density. *Phys. Rev.* **109**, 1874–1876.

PASSOT, T., SULEM, P. L. & HUNANA, P. 2012 Extending magnetohydrodynamics to the slow dynamics of collisionless plasmas. *Phys. Plasmas* **19** (8), 082113.

PESSAH, M. E., CHAN, C.-K. & PSALTIS, D. 2006 Local model for angular-momentum transport in accretion disks driven by the magnetorotational instability. *Phys. Rev. Lett.* **97** (2), 221103.

PESSAH, M. E. & GOODMAN, J. 2009 On the saturation of the magnetorotational instability via parasitic modes. *Astrophys. J.* **698** (1), L72.

POKHOTELOV, O. A., BALIKHIN, M. A., ALLEYNE, H. S.-C. K. & ONISHCHENKO, O. G. 2000 Mirror instability with finite electron temperature effects. *J. Geophys. Res.* **105**, 2393–2402.

PRAJAPATI, R. P. & CHHAJLANI, R. K. 2010 Effect of pressure anisotropy and flow velocity on Kelvin–Helmholtz instability of anisotropic magnetized plasma using generalized polytrope laws. *Phys. Plasmas* **17**, 112108.

QUATAERT, E. 1998 Particle heating by Alfvénic turbulence in hot accretion flows. *Astrophys. J.* **500** (2), 978–991.

QUATAERT, E. 2003 Radiatively inefficient accretion flow models of Sgr A*. *Astron. Nachr. Suppl.* **324**, 435–443.

QUATAERT, E., DORLAND, W. & HAMMETT, G. W. 2002 The magnetorotational instability in a collisionless plasma. *Astrophys. J.* **577** (1), 524–533.

QUATAERT, E. & GRUZINOV, A. 1999 Turbulence and particle heating in advection-dominated accretion flows. *Astrophys. J.* **520** (1), 248–255.

QUATAERT, E., HEINEMANN, T. & SPITKOVSKY, A. 2015 Linear instabilities driven by differential rotation in very weakly magnetized plasmas. *Mon. Not. R. Astron. Soc.* **447** (4), 3328–3341.

REMYA, B., REDDY, R. V., TSURUTANI, B. T., LAKHINA, G. S. & ECHER, E. 2013 Ion temperature anisotropy instabilities in planetary magnetosheaths. *J. Geophys. Res.* **118**, 785–793.

RESSLER, S. M., TCHEKHOVSKOY, A., QUATAERT, E., CHANDRA, M. & GAMMIE, C. F. 2015 Electron thermodynamics in GRMHD simulations of low-luminosity black hole accretion. *Mon. Not. R. Astron. Soc.* **454**, 1848–1870.

RINCON, F., SCHEKOCHIHIN, A. A. & COWLEY, S. C. 2015 Non-linear mirror instability. *Mon. Not. R. Astron. Soc.* **447**, L45–L49.

RIQUELME, M., OSORIO, A. & QUATAERT, E. 2017 Stochastic electron acceleration by the whistler instability in a growing magnetic field. *Astrophys. J.* **850** (2), 113.

RIQUELME, M., QUATAERT, E. & VERSCHAREN, D. 2017 PIC simulations of velocity-space instabilities in a decreasing magnetic field: viscosity and thermal conduction, arXiv:1708.03926.

RIQUELME, M. A., QUATAERT, E., SHARMA, P. & SPITKOVSKY, A. 2012 Local two-dimensional particle-in-cell simulations of the collisionless magnetorotational instability. *Astrophys. J.* **755** (1), 50.

RIQUELME, M. A., QUATAERT, E. & VERSCHAREN, D. 2015 Particle-in-cell simulations of continuously driven mirror and ion cyclotron instabilities in high beta astrophysical and heliospheric plasmas. *Astrophys. J.* **800** (1), 27.

RIQUELME, M. A., QUATAERT, E. & VERSCHAREN, D. 2016 PIC simulations of the effect of velocity space instabilities on electron viscosity and thermal conduction. *Astrophys. J.* **824** (2), 123.

ROSENBLUTH, M. N. 1956 Los Alamos Sci. *Lab. Rep.* LA-2030.

ROSIN, M. S. & MESTEL, A. J. 2012 Quasi-global galactic magnetorotational instability with braginskii viscosity. *Mon. Not. R. Astron. Soc.* **425** (1), 74–86.

ROSIN, M. S., SCHEKOCHIHIN, A. A., RINCON, F. & COWLEY, S. C. 2011 A non-linear theory of the parallel firehose and gyrothermal instabilities in a weakly collisional plasma. *Mon. Not. R. Astron. Soc.* **413** (1), 7–38.

RYAN, B. R., GAMMIE, C. F., FROMANG, S. & KESTENER, P. 2017 Resolution dependence of magnetorotational turbulence in the isothermal stratified shearing box. *Astrophys. J.* **840**, 6.

SANTOS-LIMA, R., DE GOUVEIA DAL PINO, E. M., KOWAL, G., FALCETA-GONÇALVES, D., LAZARIAN, A. & NAKWACKI, M. S. 2014 Magnetic field amplification and evolution in turbulent collisionless magnetohydrodynamics: An application to the intracluster medium. *Astrophys. J.* **781** (2), 84.

SCHEKOCHIHIN, A. A. & COWLEY, S. C. 2006 Fast growth of magnetic fields in galaxy clusters: a self-accelerating dynamo. *Astron. Nat.* **327** (5–6), 599–604.

SCHEKOCHIHIN, A. A., COWLEY, S. C., KULSRUD, R. M., ROSIN, M. S. & HEINEMANN, T. 2008 Nonlinear growth of firehose and mirror fluctuations in astrophysical plasmas. *Phys. Rev. Lett.* **100** (8), 081301.

SCHEKOCHIHIN, A. A., COWLEY, S. C., RINCON, F. & ROSIN, M. S. 2010 Magnetofluid dynamics of magnetized cosmic plasma: firehose and gyrothermal instabilities. *Mon. Not. R. Astron. Soc.* **405** (1), 291–300.

SCHMID, P. J. 2007 Nonmodal stability theory. *Annu. Rev. Fluid Mech.* **39** (1), 129–162.

SHARMA, P., HAMMETT, G. W. & QUATAERT, E. 2003 Transition from collisionless to collisional magnetorotational instability. *Astrophys. J.* **596** (2), 1121–1130.

SHARMA, P., HAMMETT, G. W., QUATAERT, E. & STONE, J. M. 2006 Shearing box simulations of the MRI in a collisionless plasma. *Astrophys. J.* **637** (2), 952–967.

SHARMA, P., QUATAERT, E., HAMMETT, G. W. & STONE, J. M. 2007 Electron heating in hot accretion flows. *Astrophys. J.* **667** (2), 714–723.

SIMON, J. B., BECKWITH, K. & ARMITAGE, P. J. 2012 Emergent mesoscale phenomena in magnetized accretion disc turbulence. *Mon. Not. R. Astron. Soc.* **422** (3), 2685–2700.

SIRONI, L. 2015 Electron heating by the ion cyclotron instability in collisionless accretion flows. II. Electron heating efficiency as a function of flow conditions. *Astrophys. J.* **800**, 89.

SIRONI, L. & NARAYAN, R. 2015 Electron heating by the ion cyclotron instability in collisionless accretion flows. I. compression-driven instabilities and the electron heating mechanism. *Astrophys. J.* **800** (2), 88.

SNYDER, P. B., HAMMETT, G. W. & DORLAND, W. 1997 Landau fluid models of collisionless magnetohydrodynamics. *Phys. Plasmas* **4** (1), 3974–3985.

SOUTHWOOD, D. J. & KIVELSON, M. G. 1993 Mirror instability. I – physical mechanism of linear instability. *J. Geophys. Res.* **98**, 9181–9187.

SQUIRE, J. & BHATTACHARJEE, A. 2014a Magnetorotational instability: nonmodal growth and the relationship of global modes to the shearing box. *Astrophys. J.* **797** (1), 67.

SQUIRE, J. & BHATTACHARJEE, A. 2014b Nonmodal growth of the magnetorotational instability. *Phys. Rev. Lett.* **113** (2), 025006.

SQUIRE, J. & BHATTACHARJEE, A. 2016 The magnetic shear-current effect: generation of large-scale magnetic fields by the small-scale dynamo. *J. Plasma Phys.* **82** (2), 535820201.

SQUIRE, J., QUATAERT, E. & SCHEKOCHIHIN, A. A. 2016 A stringent limit on the amplitude of Alfvénic perturbations in high-beta low-collisionality plasmas. *Astrophys. J.* **830** (2), L25.

SQUIRE, J., SCHEKOCHIHIN, A. A. & QUATAERT, E. 2017 Amplitude limits and nonlinear damping of shear-Alfvén waves in high-beta low-collisionality plasmas. *New J. Phys.* **19** (5), 055005-34.

VASIL, G. M. 2015 On the magnetorotational instability and elastic buckling. *Proc. R. Soc. Lond.* A **471**, 20140699.

VERSCHAREN, D., CHANDRAN, B. D. G., KLEIN, K. G. & QUATAERT, E. 2016 Collisionless isotropization of the solar-wind protons by compressive fluctuations and plasma instabilities. *Astrophys. J.* **831** (2), 128.

YOON, P. H., WU, C. S. & DE ASSIS, A. S. 1993 Effect of finite ion gyroradius on the firehose instability in a high beta plasma. *Phys. Fluids* B **5** (7), 1971–1979.

YUAN, F. & NARAYAN, R. 2014 Hot accretion flows around black holes. *Annu. Rev. Astron. Astrophys.* **52**, 529–588.